sustainability

MDPI

Article

Zeta/Flyback Hybrid Converter for Solar Power Applications

Sheng-Yu Tseng * and Jun-Hao Fan

Department of Electrical Engineering, Chang Gung University, Taoyuan 33302, Taiwan; m0921014@cgu.edu.tw
* Correspondence: sytseng@mail.cgu.edu.tw; Tel.: +886-3-2118800 (ext. 5706)

Abstract: This paper presents a zeta/flyback hybrid converter with a PV array as its power source for an LED street light or digital signage application. When the PV array is used in a LED lighting system, it needs a battery charger and discharger. In order to increase the areas of application for different PV arrays, a zeta converter has been adopted as the battery charger. In addition, since a flyback converter has a simpler circuit, it is used as the battery discharger. Due to the leakage inductor of the transformer in the flyback converter, an active clamp circuit is used to recover the energy stored in leakage inductance. Zeta and flyback converters use switch integration techniques to form the proposed zeta/flyback hybrid converter. With this approach, the proposed system has less components, a lighter weight, a smaller size, and higher conversion efficiency. Finally, a prototype of the proposed hybrid converter with an output voltage of 12 V and output power of 50 W has been implemented to verify its feasibility. It is suitable for LED lighting system applications.

Keywords: LED street light; digital signage; zeta converter; flyback converter; active clamp circuit

check for updates

Citation: Tseng, S.-Y.; Fan, J.-H. Zeta/Flyback Hybrid Converter for Solar Power Applications. *Sustainability* **2022**, *14*, 2924. https://doi.org/10.3390/su14052924

Academic Editors: Yu-En Wu and Chun-An Cheng

Received: 7 January 2022
Accepted: 17 February 2022
Published: 2 March 2022

Publisher's Note: MDPI stays neutral with regard to jurisdictional claims in published maps and institutional affiliations.

1. Introduction

Nowadays, due to the progress in material science, the performances of light-emitting diodes (LED) have been significantly improved. They have several merits, which include high brightness, a long lifetime, a small size, low maintenance, and high efficiency. Therefore, LEDs have gradually replaced traditional lighting equipment in our daily life [1–3]. They are applied to both indoor and outdoor energy-saving lighting systems, such as automotive taillights, traffic signals, streetlights, digital signage, electronic indicator boards, and so on.

In general, electricity generation uses fossil fuels, resulting in environmental pollution and a serious greenhouse effect, which disturbs the balance of the global climate. Due to zero pollution and clean energy research, renewable energy sources have been rapidly developed. In particular, solar power serves as an alternative energy source [4–6]. In previous research [4,5], renewable energy was adopted to generate utility line source. Another paper [6] proposed a soft-switching dc–dc converter for high voltage gain applications. In this paper, the proposed power system was used in LED lighting and solar power to achieve the saving of energy and carbon reduction.

When solar power is regarded as input power source of streetlights, digital signage, or electronic indicator boards, the power processer needs a battery to store energy during the day and release energy during night. Therefore, the proposed power system includes a charger and a discharger, as shown in Figure 1. Since the proposed system operating in the charging condition belongs to a low-power-level application, it can use a basic converter as its charging converter, such as buck, boost, buck–boost, cuk, zeta, and sepic converters [7–10]. In one paper [7], the proposed converter uses cuk, zeta, or sepic converters operating in the critical conduction mode (CRM) to achieve zero-current or zero-voltage switching (ZCS or ZVS). The authors of [8] proposed a simple converter, such as buck, boost, etc., to implement the renewable energy application, while [9] used a buck–boost, dc–dc converter to increase voltage gain. In addition, [10] presented a buck–boost–buck type converter to drive LED lighting. Since buck or boost converters can be operated in the

step-up or step-down voltage condition, they are not suitable for solar power applications due to the various output voltages of solar power. When a power processor uses cuk or sepic converters to transfer energy to the load, they are suitable for the step-up voltage condition due to their input port having the boost type. In addition, although buck–boost converters can implement step-down or step-up voltage functions, their power processing capability is low. They are not suitable for a higher power level application (≥100 W) [11]. Therefore, since the zeta converter possesses step-down or step-up voltage function, it was selected as the charger in the proposed converter, as shown in Figure 2.

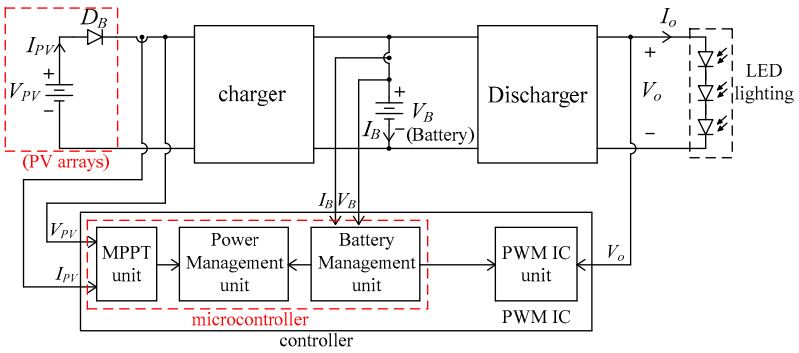

Figure 1. Block diagram of the proposed power system for solar power applications.

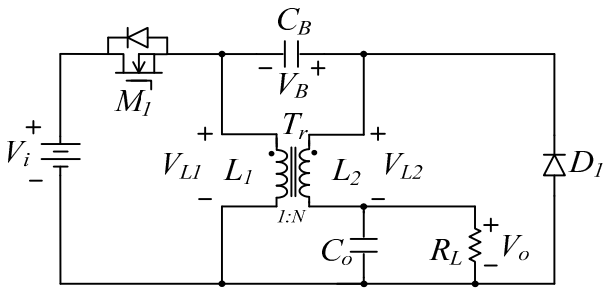

Figure 2. Schematic diagram of zeta converter with coupling inductor circuit.

Since the output voltage of a lithium battery varies from 2.5 to 4.2 V for each battery cell, its discharger needs a voltage range converter with a wide input. In addition, the proposed power system belongs to a low power level application. Therefore, a flyback or forward converter can be regarded as its discharger [12–16]. In [12,13], a flyback converter was adopted to balance each battery cell of a battery pack. Research reported in [14,15] presented a battery charger with a flyback converter. Due to simpler circuit topology, wider input voltage range, and lower cost, the flyback converter was selected as the battery discharger, as shown in Figure 3. In Figure 3, the active clamp circuit can recover the energy trapped in the leakage inductor and the help switch operating in zero-voltage switching (ZVS) at turn-on transition. Therefore, the proposed power system adopts a zeta converter as the charger and uses active clamp flyback converter as the discharger, as shown in Figure 4.

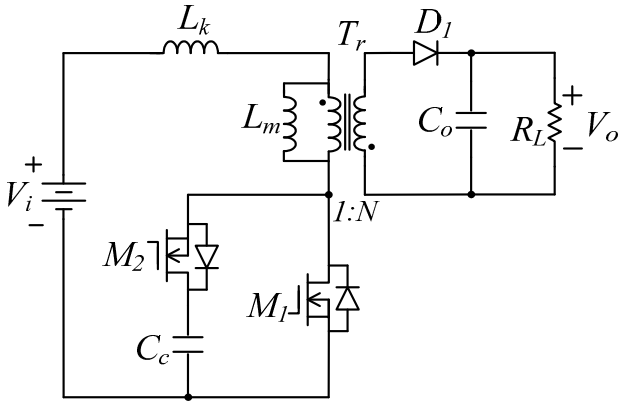

Figure 3. Schematic diagram of a flyback converter with the active clamp circuit.

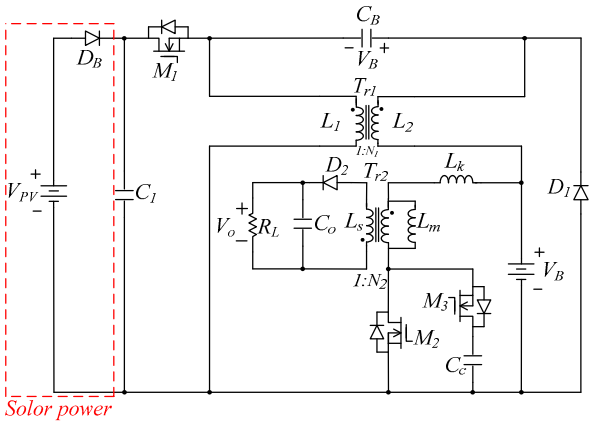

Figure 4. Schematic diagram of the conventional zeta/flyback hybrid converter.

When the proposed power system consists of zeta and flyback converters, it needs more components and a greater cost to implement the battery charging and discharging functions. Since the charger and discharger are operated at different times and their operation exchange time is long, a low-speed and low-cost switch is used to control two operational conditions: the charging condition and the discharging condition. Therefore, two sets of converters can be integrated to form a hybrid converter, as shown in Figure 5. From Figure 5, it can be seen that the proposed hybrid converter can use less components to implement the battery charging and discharging functions simultaneously. Moreover, the proposed one can be operated in ZVS at turn-on transition to increase conversion efficiency. It is suitable for the solar power system.

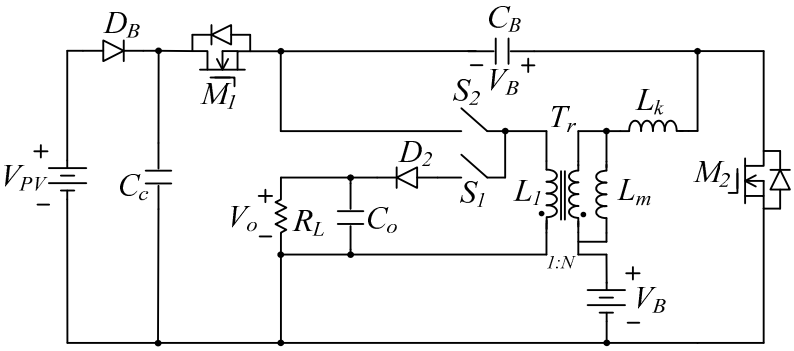

Figure 5. Schematic diagram of the proposed zeta/flyback hybrid converter.

The dc–dc converters with dual input ports and a single output port have been widely used to generate electric power for different loads [16–18] in the PV and battery system.

With the implementation of multiple input power sources, the components needed to construct these converters have been increased, resulting more complex driving circuits. Hence, a hybrid converter with three-ports, two inputs and one output, has been proposed and shown in Figure 5. Comparisons of components needed among the proposed hybrid converter and those converters provided in [16–18] are illustrated in Table 1. From Table 1, it revealed that the proposed converter needed less components to achieve the same functions of dual inputs and a single output as its compared ones; that is, only a transformer, two switches, three capacitors, and one extra switch (relay) have been used.

Table 1. Comparisons of component needed between the proposed hybrid converter and its compared ones.

Three-Port Converter	Input Ports	Output Ports	Inductors	Transformers	Switches	Diodes	Capacitors	Extra Switches
M. Kumar, et al. [16]	2	1	2	0	3	3	3	0
H. Wu, et al. [17]	2	1	3	0	3	3	1	0
Y-E. Wu, et al. [18]	2	1	1	1	4	2	3	0
The proposed Hybrid converter (Figure 5)	2	1	0	1	2	0	3	1 (relay)

2. Derivation of the Proposed Hybrid Converter

The procedures for simplifying the conventional zeta /flyback converter in Figure 4 are listed below.

- Procedure 1: As shown Figure 6a, the bidirectional circuit structure for the zeta converter with the coupling inductor circuit and flyback converter with the active clamp circuit have been used to simplify the conventional converter for the proposed power system.
- Procedure 2: Since the switches M_2 and M_{D1} in Figure 6a are operated synchronously, they can be merged to form switch M_{2D1} shown in Figure 6b. Simultaneously, a switch S_1 with a low speed and a low cost is added to the zeta and flyback hybrid converters to control the operational condition of the proposed power system. Moreover, magnetizing the inductances of transformers T_{r1} and T_{r2} has been integrated into magnetizing inductance L_{2m}.
- Procedure 3: Since voltage difference between nodes B and A is equal to V_B, the branch of switch M_3 and capacitor C_C can be moved from node B to node A, except that voltage stresses of switch M_3 and capacitor C_C are simultaneously changed, as shown in Figure 6c.
- Procedure 4: Since switches M_2 and M_3 are operated in complementary, and switches M_1 and M_{D1} are also operated in complementary, switches M_1 and M_3 are operated synchronously due to the synchronous operations of switches M_2 and M_{D1}. Therefore, switches M_3 and M_1 are integrated into switch M_{31}, and capacitors C_1 and C_C are connected in parallel to be merged as capacitor C_{C1}. In addition, inductors L_1 and L_S can be integrated with inductor L_{1S}. In order to keep the same operational principle of the proposed power system, a switch S_2 with a low speed is adopted to control different operational conditions of the proposed one. When switches S_1 and S_2 are adopted in the proposed hybrid converter and operated in complementary, a relay with a normal close and a normal open contacts can be used to realize the proposed operational conditions, as shown in Figure 6d. In Figure 6d, symbols of component devices are complex expression. They have been renamed for easy use in further explanation of operational principles of the proposed converter, as shown in Figure 5.

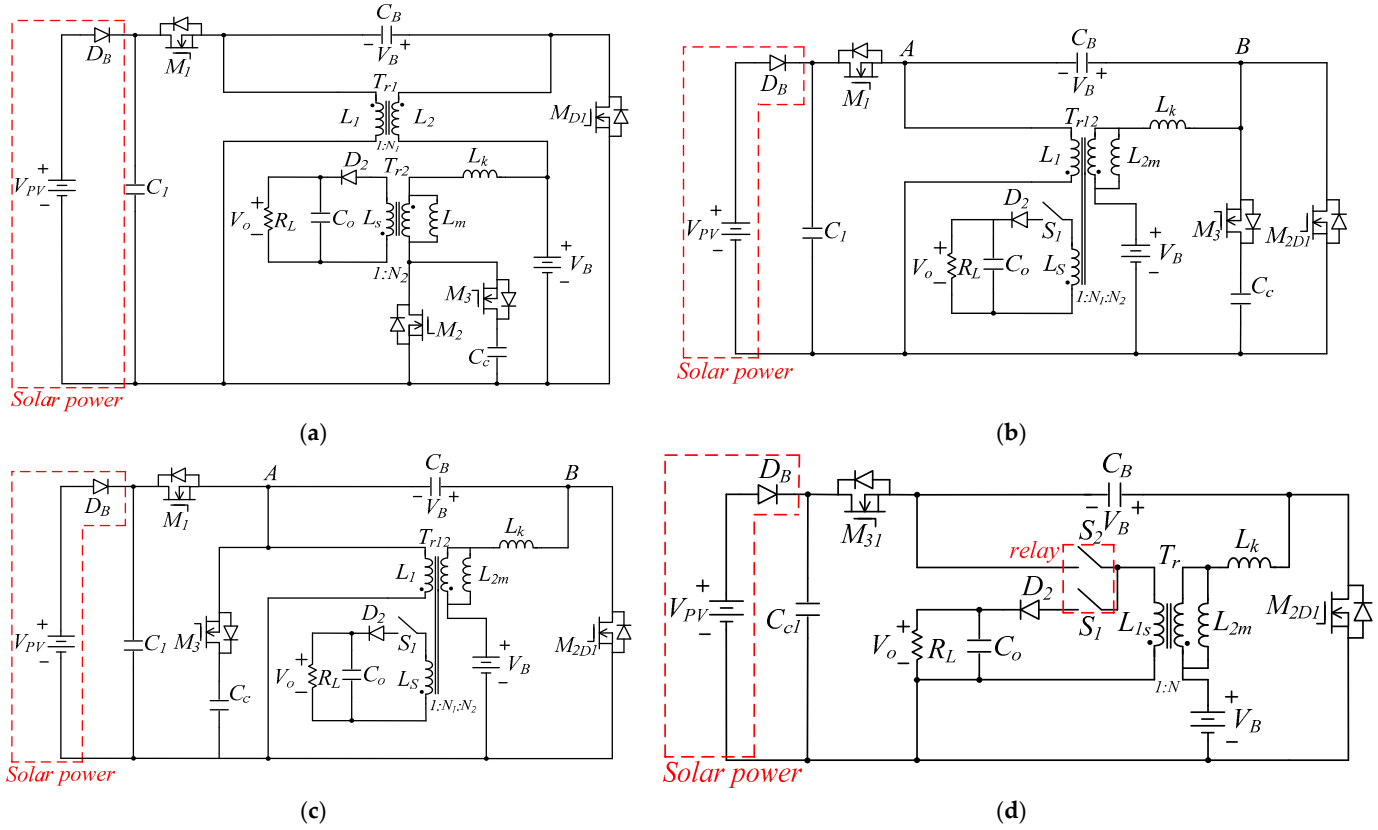

Figure 6. Circuit derivation of the proposed zeta/flyback hybrid converter: (**a**) procedure 1, (**b**) procedure 2, (**c**) procedure 3, and (**d**) procedure 4.

3. Operational Principle of the Proposed Hybrid Converter

The proposed hybrid converter can be operated in battery charging and discharging conditions, separately. Their equivalent circuits are respectively illustrated in Figure 7a,b with blue lines. Figure 7a shows a zeta converter with a coupling inductor circuit, which is used as the battery charger, while Figure 7b shows a flyback converter with an active clamp circuit, which is regarded as the battery discharger. In order to explain the operational principles of the proposed hybrid converter, operational principles of zeta and flyback converters are separately described as follows.

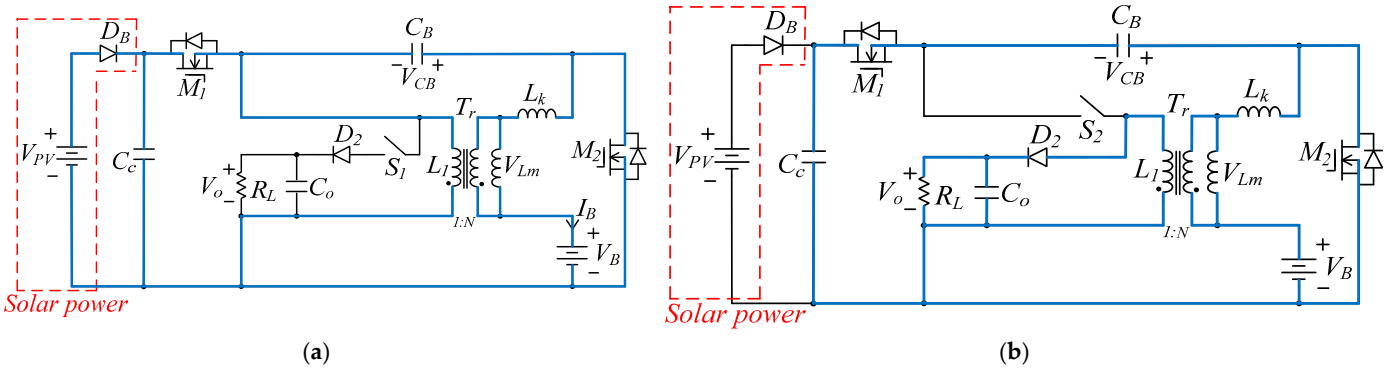

Figure 7. Wquivalent circuits of the proposed zeta/flyback hybrid converter operated in (**a**) battery charger and (**b**) battery discharger.

3.1. Battery Charger: Zeta Converter

The proposed hybrid converter adopts a zeta converter as the battery charger. Since the proposed one is always operated in the continuous conduction mode (*CCM*) from light load to heavy load, operational principles of the zeta converter with *CCM* are described in this paper. According to the operational principles of the zeta converter, the operational modes can be divided into five modes. Figure 8 illustrates the equivalent circuit of each operational mode during a completely switching cycle, while Figure 9 shows conceptual waveforms of each operational mode of the zeta converter. In the following, each operational mode is explained.

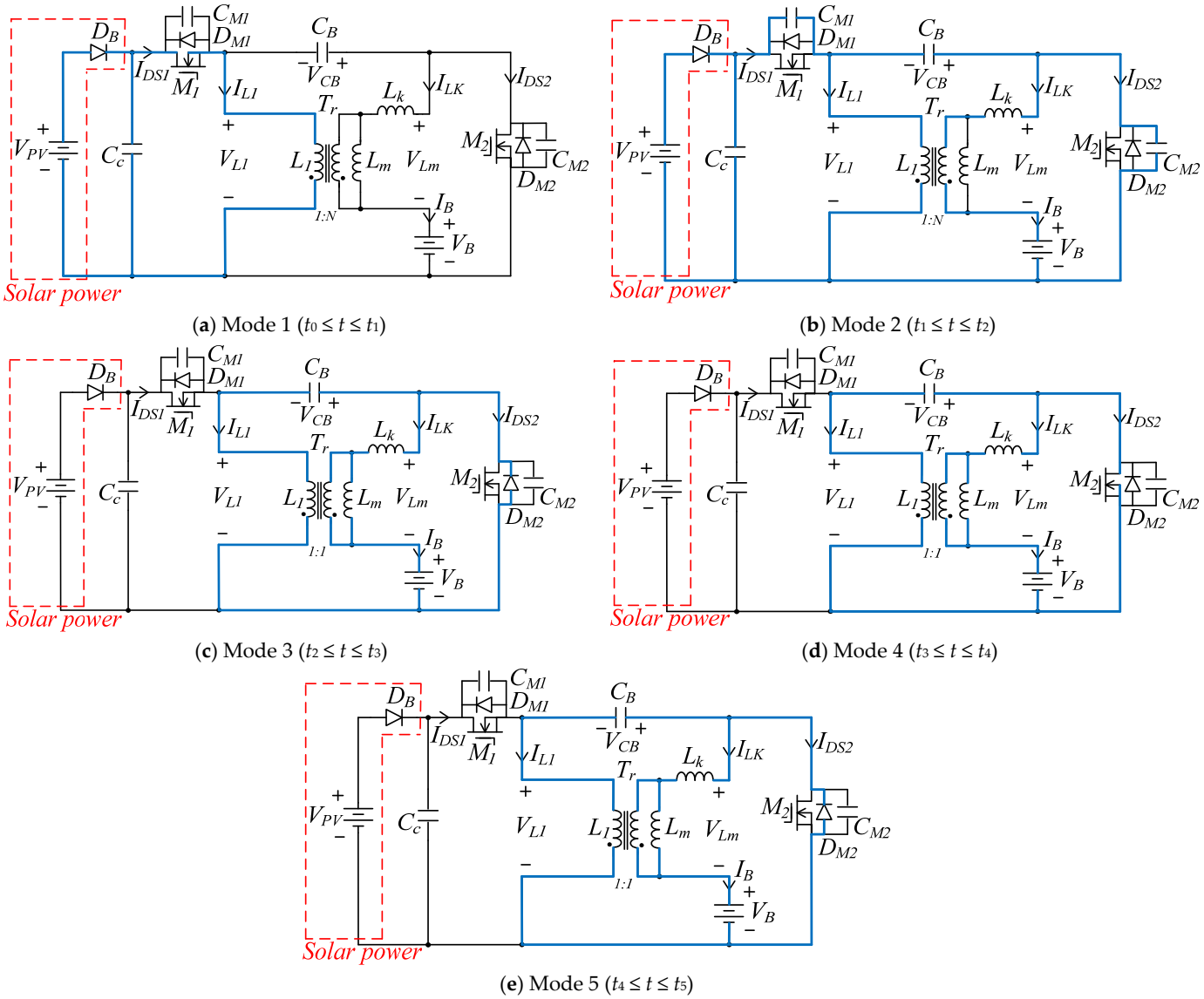

(**a**) Mode 1 ($t_0 \le t \le t_1$)

(**b**) Mode 2 ($t_1 \le t \le t_2$)

(**c**) Mode 3 ($t_2 \le t \le t_3$)

(**d**) Mode 4 ($t_3 \le t \le t_4$)

(**e**) Mode 5 ($t_4 \le t \le t_5$)

Figure 8. Equivalent circuits of each operational mode of the proposed zeta/flyback hybrid converter operated in the battery charger.

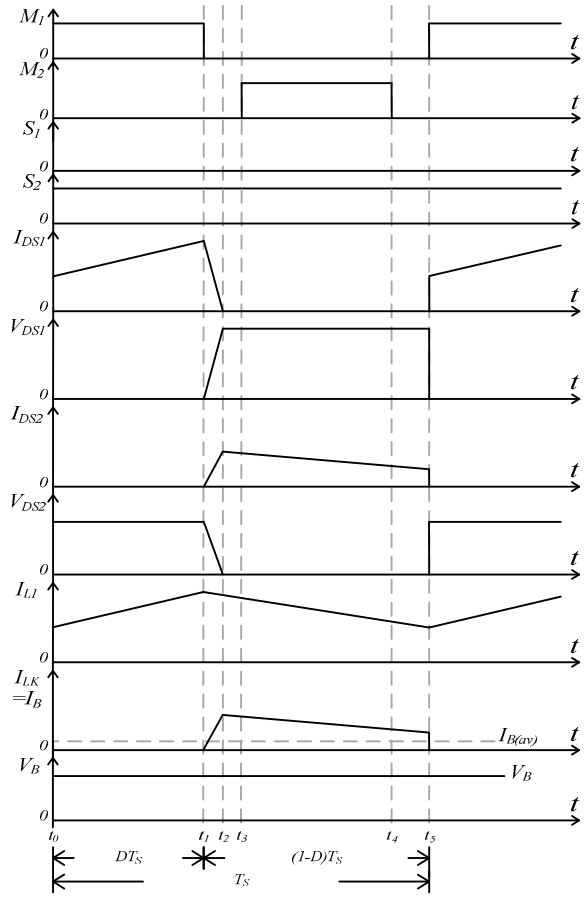

Figure 9. Conceptual waveforms of each operational mode of the proposed zeta/flyback hybrid converter operated in the battery charging condition over a completely switching cycle.

Mode 1 [Figure 8a; $t_0 \leq t < t_1$]: Before t_o, switches M_1 and M_2 are simultaneously in the off state. Since inductor current I_{Lk} is equal to $-(1/2)I_{DS2}$ and switch current I_{DS2} is a negative value, the diode D_{M2} is in the forwardly bias state. When $t = t_0$, switch M_1 is turned on and switch M_2 is still kept in the off state. At the moment, switch current I_{DS1} abruptly increases from 0 to the minimum value of inductor current I_{L1} operated in *CCM*. Therefore, diode D_{M2} is reversely biased. During this time interval, switch current I_{DS1} is equal to inductor currents (I_{L1} + I_{Lk}). Inductor currents I_{L1} and I_{Lk} linearly increases, simultaneously. Inductors L_1 and L_m simultaneously remain in the storage state.

Mode 2 [Figure 8b; $t_1 \leq t < t_2$]: At t_1, switch M_1 is turned off, and switch M_2 is still kept in the off state. Due to the continuous feature of inductor L_1, capacitor C_{M1} is charged from 0 V to $[V_{PV}/(1-D)]$, while capacitor C_{M2} is discharged from $[V_{PV}/(1-D)]$ to 0 V.

Mode 3 [Figure 8c; $t_2 \leq t < t_3$]: When $t = t_2$, switches M_1 and M_2 are in the off states. In this moment, since capacitor voltage V_{DS2} is clamped at 0 V, the diode D_{M2} is forwardly biased. Within this time interval, the inductor L_1 starts to release energy through the diode D_{M2} to the capacitor C_B. Inductor current I_{L1} linearly decreases, while inductor current I_{LK} linearly decreases to release the energy stored in the inductor L_m to the battery.

Mode 4 [Figure 8d; $t_3 \leq t < t_4$]: At t_4, switch M_1 is sustained in the off state, switch M_2 is turned on. Since the diode D_{M2} is still kept in the forwardly bias state before switch M_2 is turned on, the switch M_2 can be operated with zero-voltage switching (ZVS) at turn-on transition. In this mode, the inductor L_1 is sustained in the released energy state. Its energy flows through the switch M_2 to the capacitor C_B. The energy stored in the inductor L_m is released by the switch M_2 to the battery. Inductor currents I_{L1} and I_{Lm} linearly decrease, simultaneously.

Mode 5 [Figure 8e; $t_4 \leq t < t_5$]: A $t = t_4$, the switch M_1 is in the off state, while the switch M_2 is turned off. Since inductor currents I_{L1} and I_{Lm} must be kept in the continuous conduction condition, currents I_{L1} and I_{Lm} simultaneously flow through the diode D_{M2} to sustain their continuous conditions. When $t = t_5$, the switch M_1 is turned on again. A new switching cycle will start.

3.2. Battery Discharger: Flyback Converter

In the battery discharger condition, the proposed hybrid converter is equivalent to the flyback converter with an active clamp circuit. When load current I_o is greater than 10~20% of the full-load condition, the inductor L_m will be operated in *CCM*. Therefore, the proposed active clamp flyback converter is always operated in *CCM* under load changes from light load to heavy load.

When the active clamp flyback converter is operated in *CCM*, according to operational principles of the one, the operational modes can be divided into nine modes within a completely switching cycle. Figure 10 illustrates the equivalent circuits of each operational mode of the proposed one. Its conceptual waveforms are shown in Figure 11. In the following, each operational mode is briefly explained.

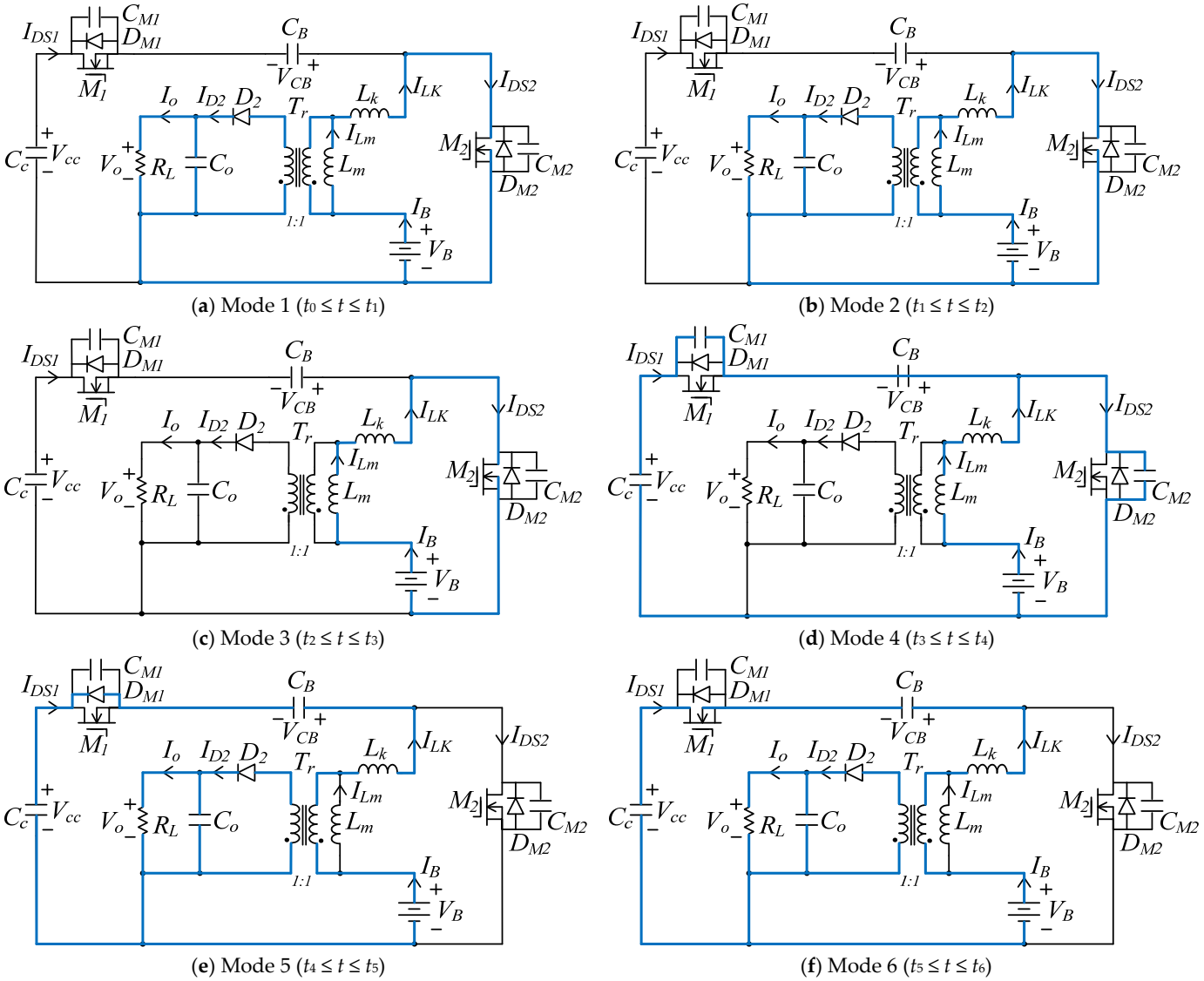

(**a**) Mode 1 ($t_0 \leq t \leq t_1$) (**b**) Mode 2 ($t_1 \leq t \leq t_2$)

(**c**) Mode 3 ($t_2 \leq t \leq t_3$) (**d**) Mode 4 ($t_3 \leq t \leq t_4$)

(**e**) Mode 5 ($t_4 \leq t \leq t_5$) (**f**) Mode 6 ($t_5 \leq t \leq t_6$)

Figure 10. *Cont.*

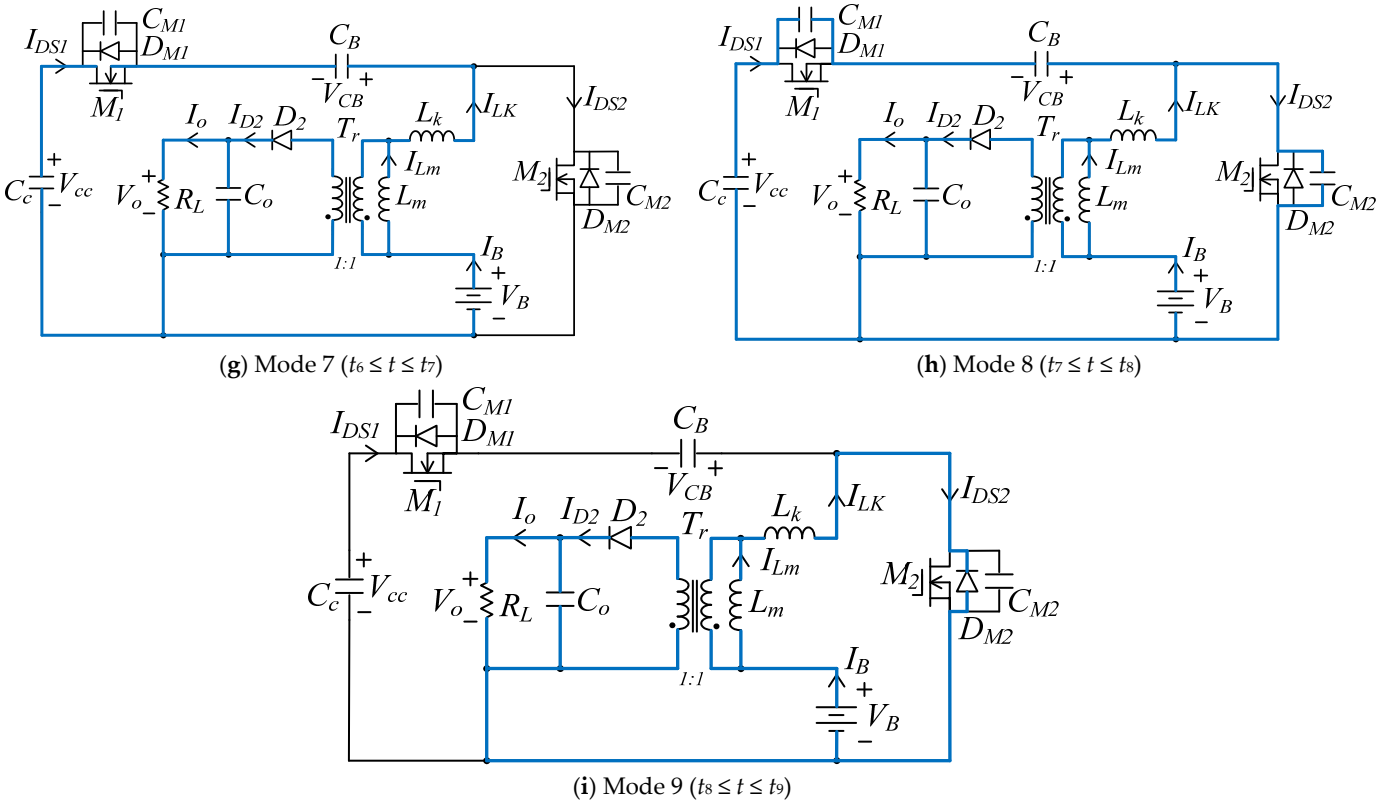

(**g**) Mode 7 ($t_6 \le t \le t_7$)

(**h**) Mode 8 ($t_7 \le t \le t_8$)

(**i**) Mode 9 ($t_8 \le t \le t_9$)

Figure 10. Equivalent circuits of each operational mode of the proposed zeta/flyback hybrid converter operated in the battery discharging condition.

Mode 1 [Figure 10a; $t_0 \le t < t_1$]: Since current I_{LK} is equal to current I_{DS2}, and its value is a negative value before t_o, the diode D_{M2} is stated in the forwardly bias condition to keep a continuous conduction condition of inductor current I_{LK}. When $t = t_0$, the switch M_1 is in the off state, while the switch M_2 is turned on. Due to the diode D_{M2} operating in the forwardly bias condition, the switch M_2 is operated with ZVS at turn-on transition. During this time interval, the energy stored in the inductor L_m is released through the transformer T_r and the diode D_2 to the load. Voltage across the secondary winding of the transformer T_r is equal to V_o. Its reflected voltage from secondary to primary windings equals V_o. Moreover, voltage, which is equal to $[V_B + (V_o)]$, is imposed on leakage inductor L_K. Since the inductance of the inductor L_K is much less than the inductance of the inductor L_m, current I_{LK} rapidly increases from a negative value to 0 A.

Mode 2 [Figure 10b; $t_1 \le t < t_2$]: When $t = t_1$, the switch M_1 is in the off state, while the switch M_2 is in the on state. In this moment, the switch current I_{DS2} is equal to 0 A. Within this time interval, the energy stored in the inductor L_m is sustained in the released energy condition, and the diode D_2 is also kept in the forwardly bias condition. In addition, voltage across the leakage inductor L_K is equal to $[V_B + (V_o)]$. Inductor current I_{LK} rapidly increases from 0 A to the minimum value, which is the minimum value of the inductor I_{Lm} operated in *CCM*.

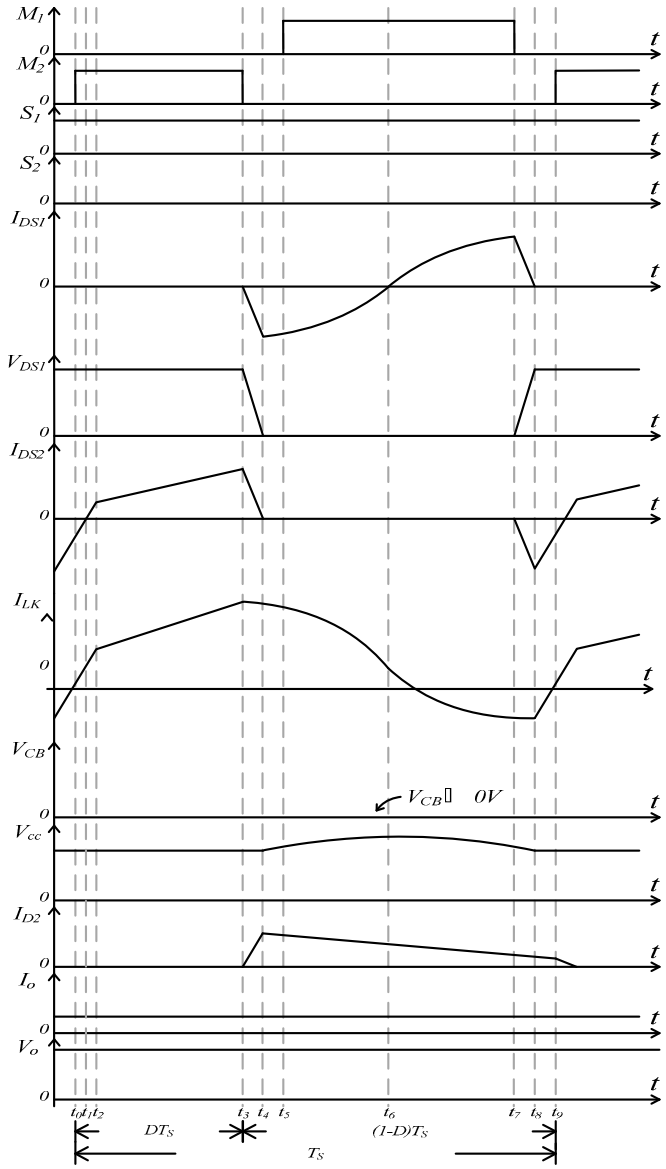

Figure 11. Conceptual waveforms of each operational mode of the zeta/flyback hybrid converter operated in the battery discharging condition over a completely switching cycle.

Mode 3 [Figure 10c; $t_2 \leq t < t_3$]: At t_2, the switch M_1 is still kept in the off state, while the switch M_2 is sustained in the on state. In this mode, the inductor L_m is worked in the energy storing state. Inductor current I_{LK} (=I_{Lm}) linearly increases.

Mode 4 [Figure 10d; $t_3 \leq t < t_4$]: When $t = t_3$, the switch M_1 is in the off state, while the switch M_2 is turned off. At the moment, inductor current I_{Lm} reaches to the maximum value. Within this time interval, since inductor current I_{LK} (=I_{Lm}) has to be kept in the continuous state, the capacitor C_{M1} is discharged from [$V_B + V_o$] to 0 V, and the capacitor C_{M2} is charged from 0 V to [$V_B + V_o$]. Since the capacitance of the capacitor C_B is much greater than that of the capacitor C_C, capacitor voltage V_{cB} is equal to 0 V, while capacitor voltage V_{CC} is kept at [$V_B + V_o$].

Mode 5 [Figure 10e; $t_4 \leq t < t_5$]: At t_4, switches M_1 and M_2 are kept in the off state. Since voltage V_{DS1} is equal to 0 V and voltage V_{DS2} is clamped to [$V_B + V_o$], the diode D_{M1} is forwardly biased. In this mode, the energy stored in the inductor L_m is released through the transformer T_r and the diode D_2 to load. Since capacitance of the capacitor C_B is much greater than that of capacitor C_C, the inductor L_K and the capacitor C_C are connected in series to form a resonant circuit. They start to generate resonance.

Mode 6 [Figure 10f; $t_5 \leq t < t_6$]: When $t = t_5$, the switch M_1 is turned on, and switch M_2 is kept in the off state. In this moment, the switch M_1 is operated with ZVS at turn-on transition since the diode D_{M1} is forwardly biased before t_5. During this time interval, the inductor L_K and the capacitor C_C are kept in the resonant condition. Inductor current I_{LK} varies in a resonant manner. Its value changes from the maximum value to 0 A. The inductor L_m is in the released energy condition. Its energy is transferred through the transformer T_r and the diode D_2 to load. Inductor current I_{Lm} linearly decreases.

Mode 7 [Figure 10g; $t_6 \leq t < t_7$]: At $t = t_6$, switch M_1 is sustained in the on state, while switch M_2 is kept in the off state. At the moment, inductor current I_{LK} is equal to 0 A. In this time interval, inductor L_K and the capacitor C_C are operated in a resonant manner, and current I_{LK} also varies in a resonant manner from 0 A to the maximum negative value. The energy stored in inductor L_m is released through the transformer T_r and diode D_2 to load. Inductor current I_{Lm} linearly decreases.

Mode 8 [Figure 10h; $t_7 \leq t < t_8$]: When $t = t_7$, switch M_1 is turned off, and switch M_2 is in the off state. During this time interval, since inductor current I_{LK} is a negative value, it causes capacitor C_{M1} to be in the charging state and capacitor C_{M2} to be in the discharging state. Therefore, capacitor voltage V_{DS1} varies from 0 V to [$V_B + V_o$], while voltage V_{DS2} changes from [$V_B + V_o$] to 0 V. Inductor L_m is under the released state, causing current I_{Lm} to linearly decrease.

Mode 9 [Figure 10i; $t_8 \leq t < t_9$]: When $t = t_8$, switches M_1 and M_2 are in the off state. At the moment, capacitor voltage V_{DS2} is clamped at 0 V. Since inductor current I_{LK} is equal to current I_{DS2} and I_{LK} is a negative value, diode D_{M2} is forwardly biased to sustain the negative value of inductor I_{LK}. During this time interval, inductor L_m is under the energy released condition. Its energy is transferred through transformer T_r and diode D_2 to load. Current I_{Lm} varies with the linear variation method. When the operational mode enters the end of mode 8, switch M_2 will be turned on again. A new switching cycle will start.

4. Design of the Proposed Hybrid Converter

The proposed hybrid converter includes a zeta converter and a flyback converter for implementing battery charging and discharging functions. In order to analyze the proposed hybrid converter, a zeta converter and a flyback converter are separately derived in this paper. In the following, the analyses of each circuit are described.

4.1. Zeta Converter

The proposed hybrid converter adopts a zeta converter for battery charger. Its equivalent circuit is shown in Figure 7a. In Figure 7a, the important parameters of the proposed circuit include duty cycle D_{11} of switch M_1, the inductance of inductor L_1, and the turns ratio N. Due to the vol-second balance of inductor L_1, the turns ratio N is equal to 1. Thus, the duty cycle D_{11} and the inductance of inductor L_1 are respectively derived as follows.

4.1.1. Duty Cycle D_{11}

Since the proposed hybrid converter uses the zeta converter as its battery charger, switch M_1 is regarded as the main switch, while switch M_2 is indicated as the auxiliary switch. In addition, a zeta converter adopts the solar power as its input source. It can transfer the solar power to the battery. In order to implement maximum power point tracking (MPPT) of the solar power, a zeta converter can regulate the charging current I_B to achieve MPPT. According to the volt-second balance of inductor L_1, the voltage of the inductor L_1 can be expressed as:

$$V_{PV} D_{11} T_s + (-V_{CB})(1 - D_{11}) T_S = 0 \quad (1)$$

where T_s is the period of a switching cycle. When switch M_1 is turned off, voltage V_{L1} of inductor L_1 is equal to capacitor voltage V_{CB}. During this time interval, since voltage V_{Lm} equals V_B, capacitor voltage V_{CB} can be rewritten by:

$$V_{CB} = \frac{V_B}{N} \tag{2}$$

where N is the turns ratio of transformer T_r. Since $N = 1$, $V_{CB} = V_B$. From (1) and (2), the transfer ratio M_{11} of a zeta converter can be derived as:

$$M_{11} = \frac{V_B}{V_{PV}} = \frac{D_{11}}{1 - D_{11}} \tag{3}$$

When a zeta converter is operated under the minimum voltage $V_{PV(min)}$ of the solar power and the maximum voltage $V_{B(max)}$ of battery. The maximum duty ratio $D_{11(max)}$ can be determined. The $D_{11(max)}$ can be expressed as:

$$D_{11(max)} = \frac{V_{B(max)}}{V_{B(max)} + V_{PV(max)}} \tag{4}$$

When the types of the solar power and battery are separately chosen, the maximum voltage $V_{PV(max)}$ can be denoted. In general, the maximum duty ratio $D_{11(max)}$ is limited at 0.7~0.8 for variations in the input voltage, components, and load. As mentioned above, since each battery possesses its own maximum charging current $I_{B(max)}$, the proposed converter can regulate charging current I_B by duty ratio D_{11} to achieve MPPT function of the solar power. The charging current I_B is limited within ranges from 0 A to $I_{B(max)}$.

4.1.2. Inductor L_1 of Transformer T_r

In general, when the proposed hybrid converter is operated in the charging condition, its equivalent circuit is the same as the zeta converter. In order to meet the volt-second balance for each inductor, voltage V_{L1} across the inductor L_1 is equal to voltage V_{Lm} across the inductor L_m. Therefore, turns ratio N is set by 1. Figure 12 shows ideal waveforms of key currents in the proposed hybrid converter operated in the battery charging condition. When the proposed one is operated in the boundary of *CCM* and discontinuous conduction mode (*DCM*), the average charging current $I_{B(av)}$ is:

$$I_{B(av)} = \frac{I_{L1(P)}}{4}(1 - D_{11}) \tag{5}$$

where $I_{L1(P)}$ is the maximum inductor current of I_{L1}. Since the proposed one is operated in the boundary, the maximum inductor current $I_{L1(P)}$ can be expressed by:

$$I_{L1(P)} = \frac{V_{PV}}{L_{1B1}}(1 - D_{11})T_s \tag{6}$$

where L_{1B1} expresses inductor L_1 operated in the boundary under charging condition. When $V_B = V_{B(max)}$ and $V_{PV} = V_{PV(min)}$, the maximum duty ratio $D_{11(max)}$ can be obtained. That is, current $I_{B(av)}$ can be rewritten by:

$$I_{B(av)} = \frac{V_{PV(min)}\left(1 - D_{11(max)}\right)^2 T_s}{4L_{1(P)}} \tag{7}$$

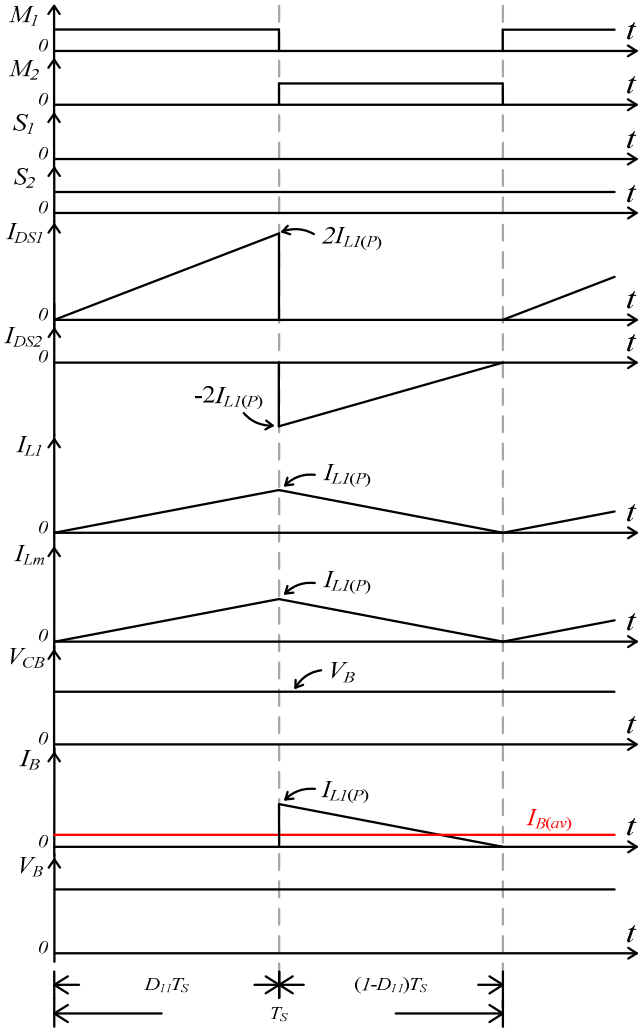

Figure 12. Ideal waveforms of key currents in the proposed hybrid converter operated in the battery charging condition.

In general, the proposed converter is designed by using the rule of thumb. The proposed one is always operated in *CCM*. That is, the proposed one under light load condition enters the operational state of *CCM*. From (7), it can be seen that average current $I_{B(av)}$ can be set by $K_1 I_{B(max)}$, where K_1 varies from 0 to 1. According to the rule of thumb of the converter design, a better range for K_1 is from 0.1 to 0.3. Therefore, inductor L_1 can be determined by:

$$L_1 = \frac{V_{PV(min)} \left(1 - D_{11(max)}\right)^2 T_s}{4K_1 I_{B(max)}} \tag{8}$$

In (8), when the types of battery and the solar power are specified, the maximum current $I_{B(max)}$ and the minimum voltage $V_{PV(min)}$ can be obtained. Therefore, the inductance of the inductors L_1 can be determined by (8).

4.2. Active Clamp Flyback Converter

When the proposed hybrid converter is operated in the discharging condition, it is equivalent to the active clamp flyback converter. Since the active clamp circuit in the proposed hybrid converter can help the switches to achieve the soft-switching features, the conversion ratio M_{12} and design of inductor L_m will not be affected. In order to design the proposed hybrid converter, important parameters are briefly derived in the following.

4.2.1. Duty Ratio D_{12}

Due to limitation of a zeta converter under the charging condition, the turns ratio N of transformer T_r is equal to 1. According to volt-second balance of inductor L_m, the relationship between voltages V_B and V_o can be expressed as:

$$V_B D_{12} T_s + (-V_o)(1 - D_{12}) T_s = 0 \tag{9}$$

Moreover, when battery V_B is under the minimum voltage $V_{B(min)}$, the maximum duty ratio $D_{12(max)}$ can be obtained and expressed by:

$$D_{12(max)} = \frac{V_o}{V_{B(min)} + V_o} \tag{10}$$

From (10), the conversion ratio $M_{12(max)}$ can be derived as:

$$M_{12(max)} = \frac{V_o}{V_{B(min)}} = \frac{D_{12(max)}}{1 - D_{12(max)}} \tag{11}$$

4.2.2. Transformer T_r

Due to the operational principles of a zeta converter, turn ratio N is limited by 1. In order to design the magnetizing inductance L_m, output current I_o is used to obtain inductance L_m. Figure 13 illustrates ideal waveforms of key currents in the proposed hybrid converter operated in the boundary of *CCM* and *DCM* under the discharging condition. In Figure 13, the average current of $I_{D2(av)}$ can be expressed by:

$$I_{D2(av)} = \frac{I_{Lm(P)}\left(1 - D_{12}\right)}{2} \tag{12}$$

where $I_{Lm(P)}$ represents the maximum value of inductance L_m. In general, when output current I_o is equal to 20~30% of the maximum output current $I_{o(max)}$, the proposed hybrid converter is operated in the boundary of *CCM* and *DCM*. Therefore, the average current $I_{D2(av)}$ can be rewritten as:

$$I_{D2(av)} = K_2 I_{o(max)} = \frac{I_{Lm(P)}\left(1 - D_{12}\right)}{2} \tag{13}$$

where K_2 represents ratio of current I_o to the maximum current $I_{o(max)}$. Its value varies from 0 to 1. Moreover, the maximum current $I_{Lm(P)}$ gives:

$$I_{Lm(P)} = \frac{V_{B(min)}}{L_{mB}} D_{12(max)} T_s \tag{14}$$

where L_{mB} is the magnetizing inductance value of magnetizing inductor L_m operated in the boundary. As mentioned above, inductance L_m can be determined by:

$$L_m = \frac{V_{B(min)} D_{12(max)} (1 - D_{12(max)}) T_s}{2 K_2 I_{o(max)}} \tag{15}$$

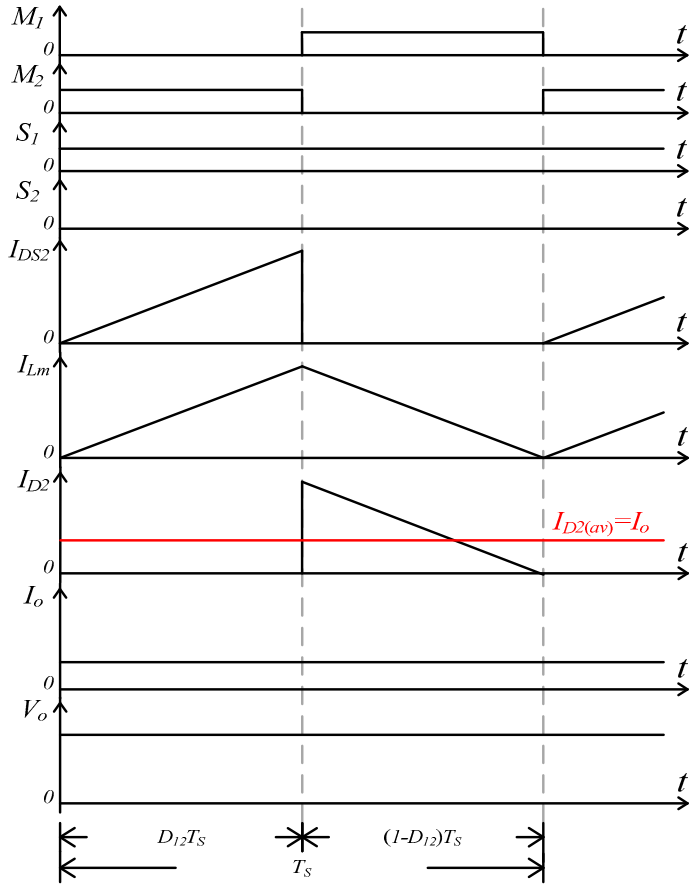

Figure 13. Ideal waveforms of key currents in the proposed hybrid converter operated in the battery discharging condition.

Since turns ratio N is equal to 1, $L_1 = L_m$. In order to determine the magnetizing inductance L_m, the maximum value can be selected between L_1 and L_m, as illustrated in (8) and (15), respectively.

4.2.3. Active Clamp Capacitor C_C

The active clamp capacitor C_C is used to recover the energy trapped in the leakage inductor L_K and help switches to implement ZVS features under the resonant manner. To achieve the soft-switching features, a half of resonant period is equal to or greater than turn-off time of the switch M_2. Therefore, the capacitor C_C has to satisfy the following inequality:

$$\pi\sqrt{C_c L_K} \geq (1 - D_{12})T_s \tag{16}$$

In (16), the capacitor C_C can be rewritten by:

$$C_c \geq \frac{(1 - D_{12})^2 T_s{}^2}{\pi^2 L_K} \tag{17}$$

From (17), it can be seen that when leakage inductance L_K is obtained by the transformer T_r, the capacitor C_C can be determined.

4.2.4. Output Capacitor C_o

In order to decrease ripples of output voltage V_o, the capacitor C_o must be large enough. The ripple voltage ΔV_o can be expressed as:

$$\Delta V_o \geq \frac{I_{o(max)} D_{12} T_s}{C_o} \tag{18}$$

where $I_{o(max)}$ is the maximum value of output current I_o. From (18), once ripple voltage ΔV_o, the maximum output current $I_{o(max)}$, duty ratio D_{12} and period T_s are determined, the output capacitor C_o can be obtained and expressed by:

$$C_o \geq \frac{I_{o(max)} D_{12} T_s}{\Delta V_o} \tag{19}$$

4.2.5. Power Loss Analysis

Since the proposed hybrid converter is operated in the discharging condition, the proposed one is operated with soft-switching manner. Its power loss analysis is the same as the flyback converter with active clamp circuit. Therefore, when the proposed hybrid converter is operated in the discharging conditions, the power losses include losses of the switches, diode, and core. In the following, power loss analyses are derived.

(1) Losses of switches

The losses of switches include switching loss and conduction loss. Figure 14 shows the conceptual waveforms of switching losses for switches M_1~M_2. Since switches M_1~M_2 are operated with *ZVS* at turn-on transition when the proposed hybrid converter is operated in the utility line condition, their switching loss is only induced at turn-off transition of the switches. Therefore, switching losses P_{soff} of switches M_1~M_2 can be expressed by:

$$P_{soff} = \frac{1}{2T_s} V_{M1(max)} (t_{off}\ I_{DP}) \tag{20}$$

where I_{DP} is the maximum current. The conduction loss of switch M_1(or M_2) can be derived as:

$$P_{DM1} = {I_{M1(rms)}}^2\ R_{DS(on)} \tag{21}$$

where $I_{M(rms)}$ is the *rms* current of each switch, and $R_{DS(on)}$ represses the resistance of the switch during the turn-on state.

(2) Loss of diode

The loss of diode D_2 is generated by the forward voltage V_F when diode D_2 is in the forward biased state. The loss P_{D2} can be derived by:

$$P_{D2} = I_{o(max)}\ V_F \tag{22}$$

(3) Loss of core

The losses of the core include core loss and copper loss. The core loss of the transformer T_r is determined by the maximum flux density B_m and the core loss curve of the core. The maximum flux density B_m can be determined by:

$$B_m = \frac{u_o u_r N_1 I_{PK}}{(l_e + u_r l_g)} \tag{23}$$

where I_{PK} is the maximum current of primary winding, N_1 expresses turns of primary winding, l_e expresses the effective magnetic path length, l_g indicates the air gap length, and u_r is the permeability. When B_m is determined, the core loss coefficient C_p can be obtained through core loss curve of core. The core loss P_{CL} is determined as:

$$P_{CL} = C_P V_e \tag{24}$$

where V_e is the effective core volume of the core. Moreover, the copper loss P_{CPL} can be derived by:

$$P_{CPL} = {I_{Lm(rms)}}^2\ R_{dc1}\ l_{m1} + {I_{D2(rms)}}^2\ R_{dc2}\ l_{m2} \tag{25}$$

where R_{dc1} is the resistance coefficient of the wire gauge of primary winding, l_{m1} represses the total length of turns of the primary winding, R_{dc2} is the resistance coefficient of the wire gauge of the secondary winding, and l_{m2} indicates the total length of turns of the secondary winding.

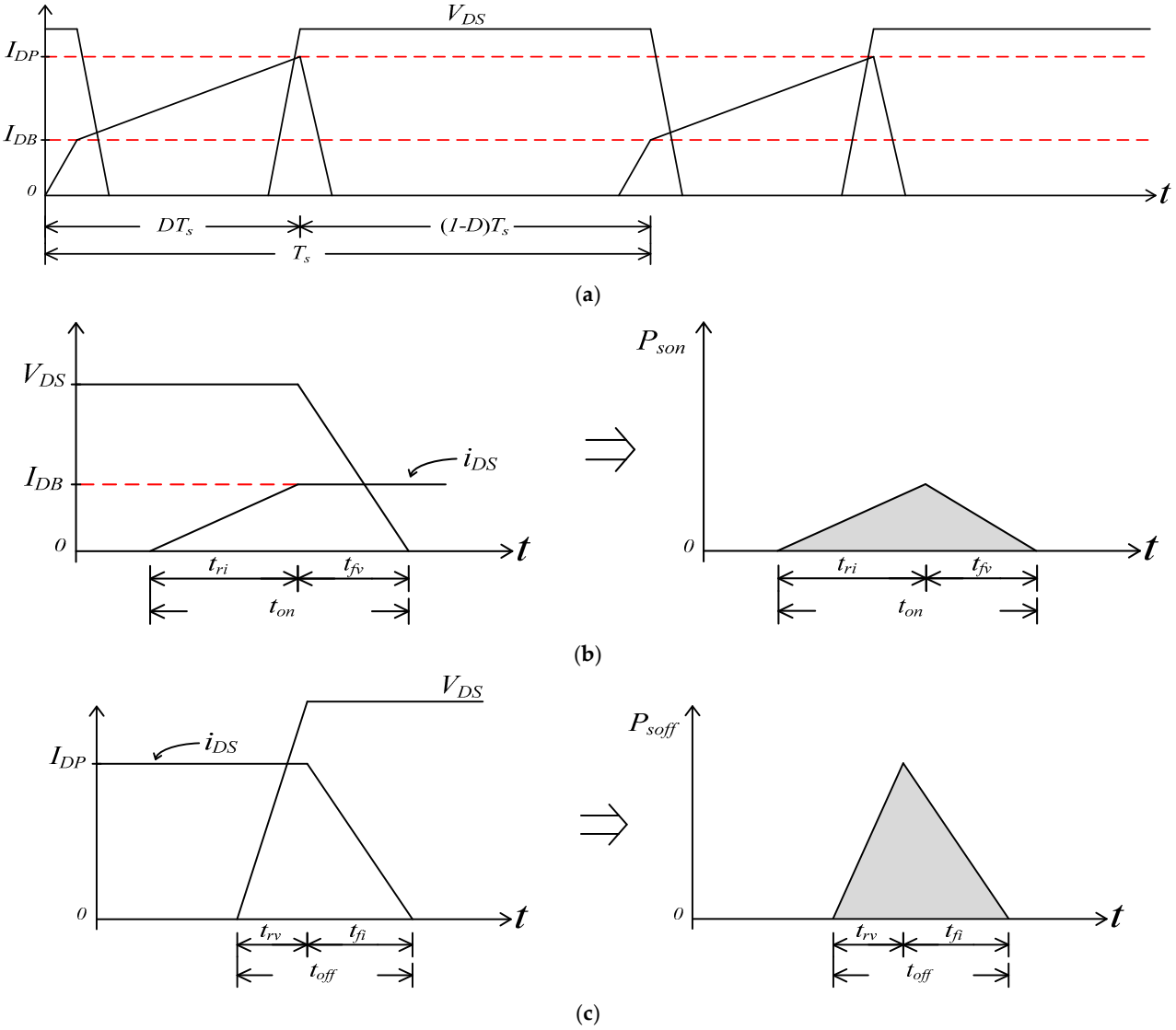

Figure 14. Conceptual waveforms of switching losses during switch turn-on and turn-off transitions (**a**) during one switching cycle, (**b**) during turn-on transition, (**c**) during turn-off transition.

5. Circuit Control of the Proposed Hybrid Converter

The circuit topology consists of charger/discharger controller, as shown in Figure 15. The charger/discharger controller is used to control the charger/discharger circuit to implement battery charging and discharging functions. In Figure 15, the charger/discharger includes a MPPT unit, a CC command selection unit. Table 2 illustrates definitions of the important parameters shown in Figure 15, while Table 3 lists the operational conditions of the controller of the proposed hybrid converter. In the following, each unit is briefly described.

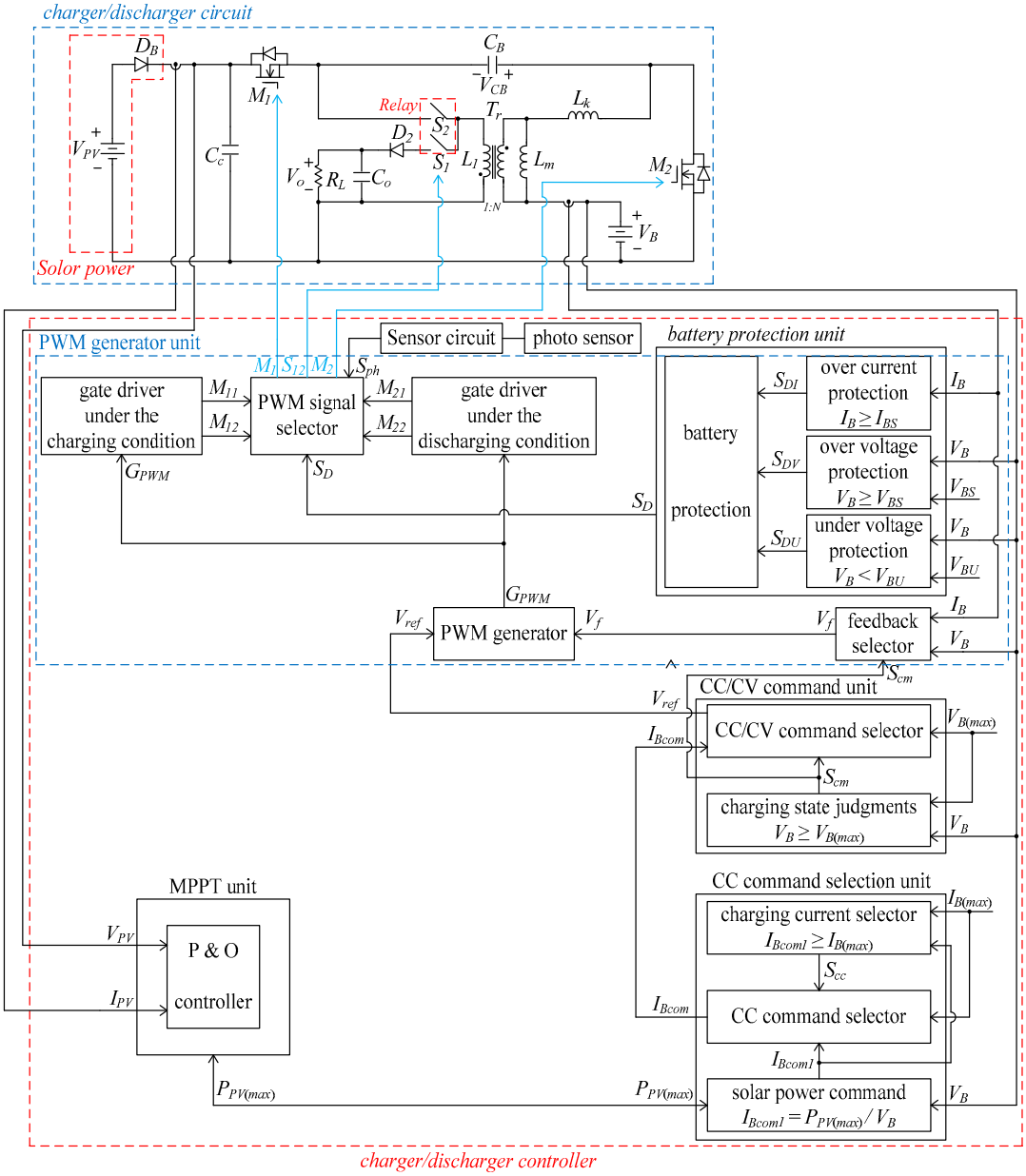

Figure 15. Block diagrams of the charger/discharger controller for the proposed hybrid converter.

Table 2. Definitions of the important parameters in Figure 15 for the charger/discharger of the proposed hybrid converter.

Symbol	Definition	Symbol	Definition
V_{PV}	output voltage of solar power	V_f	feedback signal of PWM generator
V_B	battery voltage	G_{PWM}	PWM signal of main switch
$V_{B(max)}$	maximum battery voltage	S_{DI}	protection signal of $I_B \geq I_{BS}$
V_{BS}	over voltage protection of battery	S_{DV}	protection signal of $V_B \geq V_{BS}$
V_{BU}	under voltage protection of battery	S_{DU}	protection signal of $V_B \leq V_{BU}$
I_B	battery current	S_D	protection signal of battery
$I_{B(max)}$	maximum charging/discharger current of battery	M_{11}	gate signal under the charging condition

Table 2. *Cont.*

Symbol	Definition	Symbol	Definition
I_{BS}	over current protection of battery	M_{12}	gate signal under the charging condition
$P_{PV(max)}$	maximum output power of solar power at present	M_{21}	gate signal under the discharging condition
I_{Bcom1}	current command value under $P_{PV(max)}$	M_{22}	gate signal under the discharging condition
I_{Bcom}	current command value with CC charging method	S_{ph}	photo sensor signal
S_{cc}	selecting signal of CC command	S_{12}	gate signal of switch S_1 and S_2
S_{cm}	selecting signal of CC/CV command	M_1	gate signal of switch M_1
V_{ref}	command signal of PWM generator	M_2	gate signal of switch M_2

Table 3. Operational conditions of the proposed hybrid converter for the controller shown in Figure 15.

Controlling Unit		Selection/Judgement Condition		Operational Condition
		Variable	State	
CC command selection unit	solar power command	S_{PV}		$I_{Bcom1} = \frac{P_{PV(max)}}{V_B}$
	charging current selector	S_{CC}	High	$I_{Bcom1} \geq I_{B(max)}$
			Low	$I_{Bcom1} < I_{B(max)}$
	CC command selection	I_{Bcom}	S_{cc} = High	$I_{Bcom} = I_{B(max)}$
			S_{cc} = Low	$I_{Bcom} = I_{Bcom1}$
CC/CV command selection unit	Charging state judgement	S_{cm}	High	$V_B \geq V_{B(max)}$
			Low	$V_B < V_{B(max)}$
	CC/CV command selector	V_{ref}	S_{cm} = High	$V_{ref} = V_{B(max)}$ under CV operation
			S_{cm} = Low	$V_{ref} = I_{B\text{com}}$ under CC operation
PWM generator unit	Feedback selector	V_f	S_{cm} = High	$V_f = V_B$ under CV operation
			S_{cm} = Low	$V_f = I_B$ under CC operation
	PWM generator	G_{PWM}		Error value by V_{ref} and V_f
	Gate driver under the charging condition	M_{11}		$M_{11} = S_{PWM}$
		M_{12}		$M_{12} = \overline{S_{PWM}}$
	Gate driver under the discharging condition	M_{21}		$M_{21} = \overline{S_{PWM}}$
		M_{22}		$M_{22} = S_{PWM}$
	PWM signal selector	M_1		$M_1 = M_{11}\, S_{ph} + M_{21}\, \overline{S_{ph}}$
		M_2		$M_2 = M_{12}\, S_{ph} + M_{22}\, \overline{S_{ph}}$
		S_{12}	S_{ph} = High	Under the charging condition
			S_{ph} = Low	Under the charging condition
		S_D	High	shutdown the proposed system
			Low	normal operation
Battery protection unit	Over current protection	S_{DI}	High	$I_B \geq I_{BS}$: over current protection
			Low	$I_B < I_{BS}$: normal operation
	Over voltage protection	S_{DV}	High	$V_B \geq V_{BS}$: over voltage protection
			Low	$V_B < V_{BS}$: normal operation
	Under voltage protection	S_{DU}	High	$V_B \leq V_{BU}$: under voltage protection
			Low	$V_B > V_{BU}$: normal operation
	Battery protection	S_D	High	shutdown the proposed system
			Low	normal operation

5.1. MPPT Unit

The proposed hybrid converter uses solar power to transfer power to the battery. In order to extract the maximum power of the solar power, a perturb and observe (P&O) method is adopted. The operational algorithm explained in [19] has been used in this paper, the descriptions are omitted. The MPPT unit in the charger/discharger controller is used to separately obtain voltage V_{PV} and current I_{PV} by voltage V_{PV} and current I_{PV} signals. According to the operational principles of P&O method, the MPPT unit is associated with the CC command selection unit, the CC/CV command unit and the PWM generator unit to operate the solar power at the maximum power point (MPP). That is, the maximum power can be obtained by the MPPT unit.

5.2. CC Command Selection Unit

When the proposed hybrid converter is operated in the charging condition, the CC-CV method is used to implement lithium battery charge. In general, the operational exchange time and the CC and CV methods have $V_B \geq V_{B(max)}$, where $V_{B(max)}$ represents the voltage regulation value under the CV operational condition. Therefore, the proposed hybrid converter always adopts the CC mode to charge the battery, and then the charging operational condition can be changed from CC mode to CV mode when voltage V_B is equal to or greater than voltage $V_{B(max)}$. In order to operate in a proper CC command value under the CC operational mode, the CC command selection unit first determines the CC command value I_{Bcom1} under the maximum power $P_{PV\ (max)}$ of the solar power. The CC command value I_{Bcom1} is equal to $(P_{PV\ (max)}/V_B)$. Since the charging current I_B is limited with $I_{B(max)}$, the CC command selection unit uses charging current selection to judge the relationship between I_{Bcom1} and $I_{B(max)}$. When $I_B \geq I_{B(max)}$, signal S_{cc} is in the high-level condition. If $I_{Bcom1} < I_{B(max)}$, signal S_{cc} is in the low-level condition. The signal S_{cc} is sent to the CC command selector. According to the operational condition listed in Table 2, the CC command value I_{Bcom} is equal to $I_{B(max)}$ when S_{cc} is in the high-level condition, and I_{Bcom} is equal to I_{Bcom1} as the S_{cc} is in the low-level condition. The CC command value I_{Bcom} is sent to the CC/CV command unit to be used as the reference value V_{ref} of the PWM generator under the CC operational condition.

5.3. CC/CV Command Unit

The CC/CV command unit is used to generate the command value V_{ref} for PWM generator. Since the battery charging period is divided into two intervals, while there are CC operational intervals and CV operational intervals, their command values are different. When the charging mode is in the CC operational condition, the command value V_{ref} is equal to I_{Bcom}. If the charging mode is under the CV operational condition, V_{ref} equals $V_{B(max)}$. In the CC/CV command unit, the charging state depends on voltage V_B. When $V_B \geq V_{B(max)}$, the charging state enters the CV operational condition. At this time, signal S_{cm} is in the high-level condition. Moreover, when $V_B < V_{B(max)}$, the charging state is under the CC operational condition. The signal S_{cm} is in the low-level condition. As mentioned above, the operational condition of battery is determined by the voltage level of battery. The CC/CV command unit can be used to determine the command value V_{ref} depending on the different operation condition.

5.4. PWM Generator Unit

The PWM generator unit includes a feedback selector, a PWM generator, a gate driver under the charging condition, a gate driver under the discharging condition, and a PWM signal selector. The feedback selector and the PWM generator are combined to generate PWM signal GPWM. When $V_B \geq V_{B(max)}$, signal S_{cm} is in the high-level condition, and the operational condition is in the CV charging mode. The feedback signal V_f in the feedback selector is equal to V_B and the output voltage V_{ref} of the CC/CV command selector. By comparing the error values between signals V_{ref} and V_f with triangle wave, the PWM signal GPWM can be produced. On the other hand, when signal S_{cm} is in the low-level condition,

the charging mode is operated in the CC charging mode. The command value V_{ref} equals I_{Bcom} and feedback signal V_f is equal to I_B. The signals V_{ref} and V_f are sent to the PWM generator to produce PWM signal GPWM.

The gate driver under the charging condition can generate two PWM signals M_{11} and M_{12} by GPWM. In this operational condition, signal M_{11} is equal to signal GPWM. While signal M_{12} is generated by signal GPWM in complementary. Moreover, the gate driver under the discharging condition can generate two signals, M_{21} and M_{22}, by GPWM. In this circuit, signal M_{22} equals GPWM, while signal M_{21} is generated by signal GPWM in complementary. Two pair signals, (M_{11}, M_{12}) and (M_{21}, M_{22}), are sent to the PWM signal selector to generate signals M_1 and M_2, respectively. Moreover, a photo sensor is adopted to generate signal S_{ph}. When signal S_{ph} is in the high level condition,,the proposed hybrid converter is operated in the charging condition. Signal $M_1 = M_{11}$ and $M_2 = M_{12}$. Signal S_{12} is used to drive relay. Therefore, the switch S_1 is in the off state and the switch S_2 is in the on state. If signal S_{ph} is in the low-level condition, the proposed hybrid converter is operated in the discharging condition. Signal $M_1 = M_{21}$, and $M_2 = M_{22}$. Signal S_{12} is adopted to drive relay, where te switch S_1 is in the on state and switch S_2 is in the off state. In addition, when signal S_D changes from low level to high level, the proposed hybrid converter is shut down due to operational conditions under overcurrent, overvoltage, or undervoltage protection.

5.5. Battery Protection Unit

The battery protection unit includes overcurrent, overvoltage, and undervoltage protections. When the charging or discharging current I_B is equal to or greater than the set current I_{BS}, signal S_{DI} varies from low level to high level. The operational condition is in the overcurrent condition, and the proposed hybrid converter must be shut down. If voltage V_B is equal to or greater than voltage V_{BS}, signal S_{DV} changes from the low level to high level. The operational condition is in the overvoltage condition. The proposed hybrid converter has to be shut down. In addition, when voltage V_B is equal to or less than voltage V_{BU}, the proposed hybrid converter enters the under-voltage operational condition. Signal S_{DU} is in the high-level state, and the proposed hybrid converter is shut down. Output signal S_D can be expressed by $S_{DI} + S_{DV} + S_{DU}$. When signal S_D changes from low level to high level, the PWM signal selector is disabled. That is, signals M_1, M_2, and S_{12} are in the low-level condition, simultaneously. Switches M_1, M_2, and relay are simultaneously in the off state, resulting in the proposed hybrid converter operated in the shutdown condition.

6. Experimental Results

The proposed hybrid converter is regarded as the charger and discharger. In order to verify its feasibility, a prototype was implemented by the following specifications:

A. Charger: zeta converter:
- Input voltage V_{PV}: DC13.5~22.5 V (PV array);
- Maximum input power $P_{PV(max)}$: 50 W;
- Operating frequency f_{s1}: 50 kHz;
- Maximum charging current $I_{BC(max)}$: 6 A;
- Output voltage V_B: DC5 V~8.4 V (lithium battery: 3.2 Ah).

B. Discharger: flyback converter:
- Input voltage V_B: DC5 V~8.4 V (lithium battery: 3.2 Ah);
- Maximum input current $I_{BD(max)}$: 6.8 A;
- Operating frequency f_{s2}: 50 kHz;
- Maximum output current $I_{o(max)}$: 4.2 A;
- Output voltage V_o: 12 V.

As circuit specifications mentioned above, the PV arrays adopts a maximum output power $P_{PV(max)}$ = 50 W. The important parameters of the PV arrays are listed in Table 4. Since a single battery cell possesses a lower voltage level, a number of battery calls are

connected in series to increase its output voltage capability or, in parallel, to increase its output current capability. Considering the voltage and current ratings of the battery pack, two battery cells are connected in series to form a battery string, and four battery strings are connected in parallel to form a battery pack. That is, the battery pack are combined with 2 series*4 in parallel. Its specifications are listed in Table 5. According to the circuit specifications of the proposed hybrid converter, the voltage and current stresses of switches M_1 and M_2 are 31 V/7.47 A and 31 V/9.49 A, respectively. Here, the switches M_1 and M_2 are realized by Aow 2918 with the voltage and current ratings of 100 V/90 A. In addition, the voltage and current stresses of diode D_2 are 20.4 V/7.82 A, respectively. STPS10L60D, with voltage and current ratings of 60 V/10 A, is selected for diode D_2. The selection of the key components are listed in the following.

- Switches M_1 and M_2: Aow2918;
- Capacitor C_B: 10 μF/100 V;
- Transformer T_r core: EE-33;
- Transformer T_r: L_m = 48 μH (leakage inductance L_k = 7 μH);
- Trans ratio N: 1;
- Diode D_2: STPS10L60D;
- Capacitor C_C: 0.5 μF.

Table 4. Parameters of PV arrays supplied by PV arrays manufacturer.

Parameters	Values
Maximum Power ($P_{PV(max)}$)	50 W
Maximum Power voltage ($V_{PV(max)}$)	17.96 V
Maximum Power current ($I_{PV(max)}$)	2.78 A
Open circuit voltage (V_{OC})	22.5 A
Short circuit current (I_{SC})	3.1 A

Table 5. Specifications of battery pack supplied by battery manufacturer.

Parameters	Single Battery Cell Value	Battery Pack Values (2 Series*4 Parallel)
Capacity rating	3.2 Ah	25.6 Ah
Nominal voltage	3.6 V	7.2 V
Maximum charging voltage	4.2 V	8.4 V
Standard charging current	1.625 A	6.45 A
Minimum discharging voltage	2.5 V	5.0 V
Minimum discharging current	6.4 A	25.6 A

The proposed hybrid converter can be regarded as a battery charger and discharger. In order to verify functions of the proposed hybrid converter, some experimental results are measured for battery charging or discharging. When the proposed hybrid converter is operated in the battery charging condition, Figures 16 and 17 show the measured switch voltage V_{DS} and current I_{DS} waveforms of switches M_1 and M_2. Figure 16 illustrates those waveforms under the 20% full-load condition, while Figure 17 expresses those waveforms under the 100% full-load condition. From Figures 16 and 17, it can be seen that the proposed hybrid converter can be operated in *CCM* from the 20% full-load condition to the 100% full-load condition. Figure 18 depicts measured battery voltage V_B and current I_B waveforms under different battery charging currents. Figure 18a shows those waveforms under the average charging current $I_{B(av)}$ = 2 A, while Figure 18b illustrates those waveforms under the average charging current $I_{B(av)}$ = 6 A. Figure 18 shows that the proposed hybrid converter

can operate in different charging currents I_B. In order to verify the dynamic response of the proposed hybrid converter, the charging current I_B changed with the step-load change between I_B = 0.6 A and $I_{B(max)}$ = 6 A is shown in Figure 19. From Figure 19, it can be seen that when the battery charging current I_B varies between 0.6 A and 6A, voltage V_B of battery can be kept within ±1%. By using PV arrays as the input source of the proposed hybrid converter, the perturbation and observation (P&O) method is adopted to acquire the maximum power of the PV arrays. When the MPPT of the solar power is implemented, the solar power is replaced by power supply with a function of the solar power simulation curve. Figure 20 shows measured PV arrays voltage V_{PV}, current I_{PV}, and power P_{PV} waveforms under $P_{PV(max)}$ = 50 W. In Figure 20, when PV arrays power P_{PV} varies from 0 W to 50 W, it needs about 450 ms to trace the maximum power. After t_1, PV arrays power is kept at 50 W. That is, the solar power is operated at maximum power point.

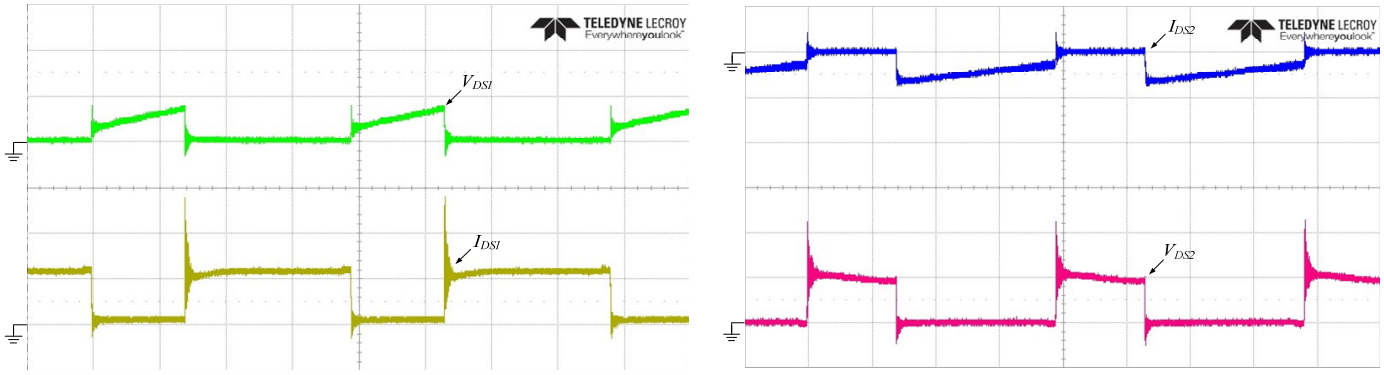

(**a**) (V_{DS1}: 20 V/div, I_{DS1}: 5 A/div, time: 5 μs/div) (**b**) (V_{DS1}: 20 V/div, I_{DS1}: 5 A/div, time: 5 μs/div)

Figure 16. Measured switch voltage V_{DS} and current I_{DS} waveforms under 20% of full-load condition: (**a**) switch M_1 and (**b**) switch M_2.

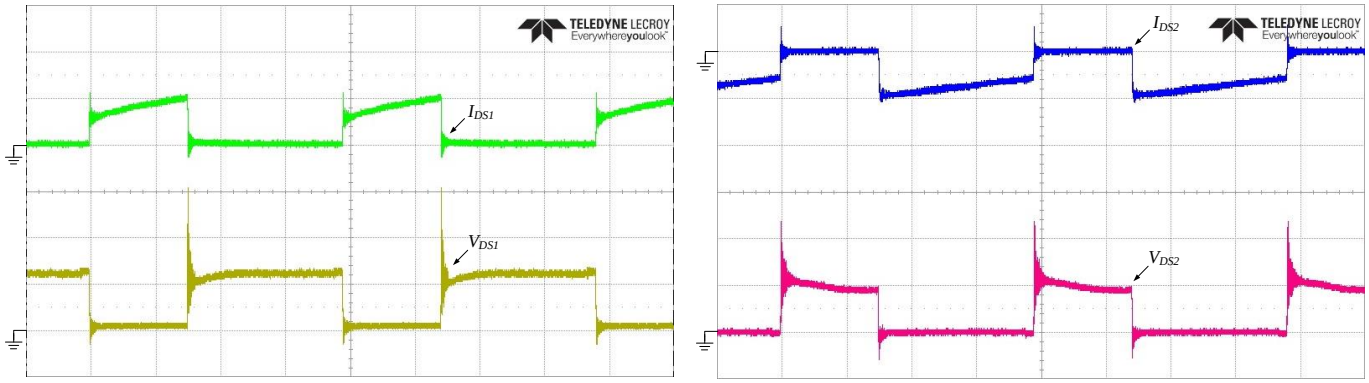

(**a**) (V_{DS1}: 20 V/div, I_{DS1}: 5 A/div, time: 5 μs/div) (**b**) (V_{DS1}: 20 V/div, I_{DS1}: 5 A/div, time: 5 μs/div)

Figure 17. Measured switch voltage V_{DS} and current I_{DS} waveforms under 100% of full-load condition: (**a**) switch M_1 and (**b**) switch M_2.

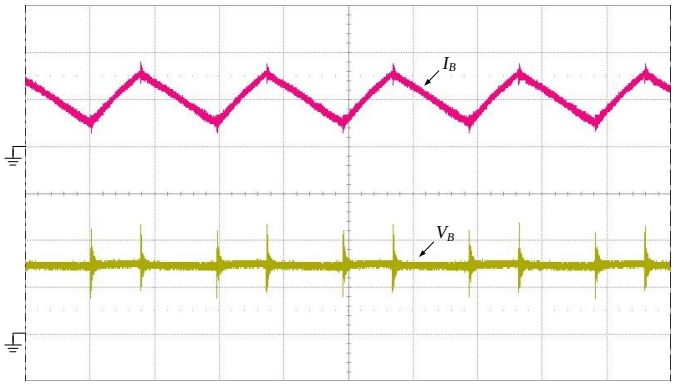

(**a**) (V_{DS1}: 5 V/div, I_{DS1}: 2 A/div, time: 10 µs/div)

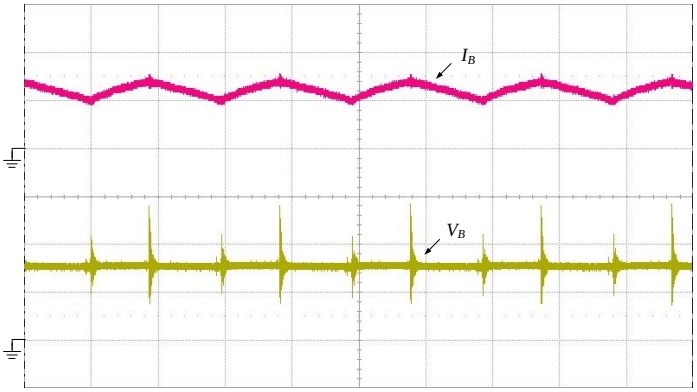

(**b**) (V_{DS1}: 5 V/div, I_{DS1}: 5 A/div, time: 10 µs/div)

Figure 18. Measured battery voltage V_B and current I_B waveforms (**a**) under I_B = 2 A and (**b**) under $I_{B(max)}$ = 6 A.

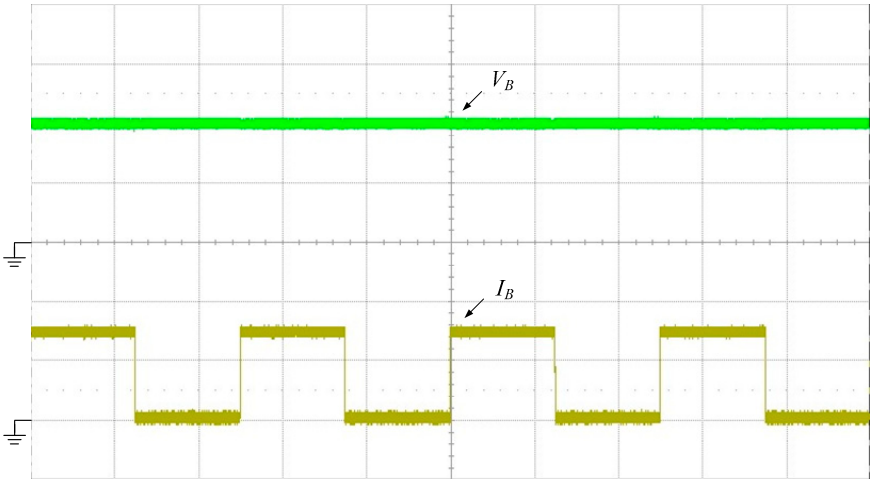

(V_B: 4 V/div, I_B: 4 A/div, time: 200 ms/div)

Figure 19. Measured battery voltage V_B and current I_B waveforms under step-load change between I_B = 0 A and $I_{B(max)}$ = 6 A.

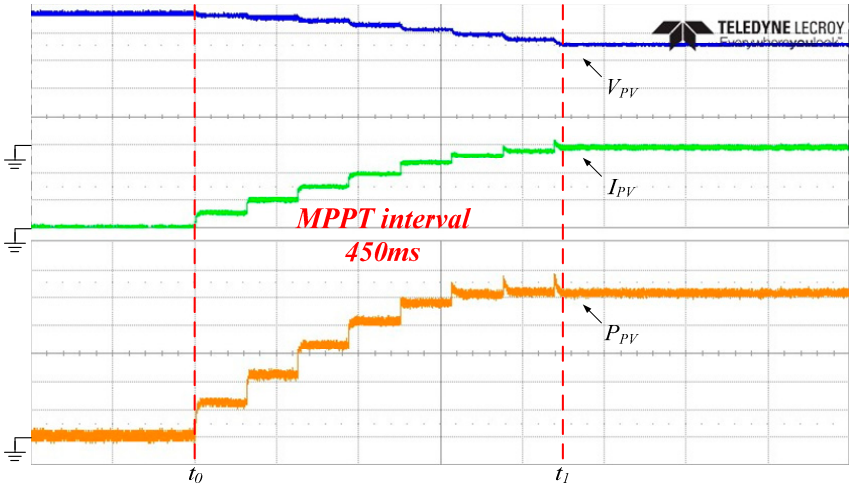

(V_{PV}: 5 V/div, I_{PV}: 1 A/div, P_{PV}: 500 ms/div)

Figure 20. Measured P_V array voltage V_{PV}, current I_{PV} and power P_{PV} under maximum P_V power $P_{PV(max)}$ = 50 W.

When the proposed hybrid converter is operated in the discharging condition, the active clamp flyback converter is used to achieve battery discharging, as shown in Figure 7b. Figures 21 and 22 illustrate that the measured switch voltage V_{DS} and current I_{DS} waveforms of the proposed hybrid converter under battery voltage V_B = 8 V. Figure 21 shows those waveforms under the 30% full-load condition, while Figure 22 indicates those waveforms under the 100% full-load condition. From Figures 21 and 22, it can be observed that switches M_1 and M_2 are approximately operated with ZVS at turn-on transition under the 30% full-load condition. That is, soft-switching ranges of the proposed hybrid converter operated in the discharging condition are depicted from 30% to 100% of the full-load condition. Figure 23 illustrates the measured output voltage V_o and current I_o waveforms of the proposed hybrid converter under step-load changes between I_o = 0 A and I_o = 4 A. When load current I_o varies between 0 A and 4 A, the output voltage variation ΔV_o is limited within ±1%. That is, the proposed hybrid converter possesses a good dynamic response. Figure 24 shows the efficiency comparison between a flyback converter with a hard-switching circuit and with the proposed active clamp circuit from light load to heavy load. In Figure 24, the conversion efficiency of the flyback converter with the proposed active clamp circuit under 100% of full-load condition is about 87%. It is 4% more efficiency than that of a flyback converter with a hard-switching circuit under a 100% full-load condition. The total power loss under the full-load condition equals 7.52 w. According to power loss analysis, the driving circuit is about 2.8% of the total power loss. Losses of switches are approximated to be 36% of the total power loss; the losses of diode D_2 are about 31.2% of the total power loss; while losses of transformer T_r are approximately 30% of the total power loss.

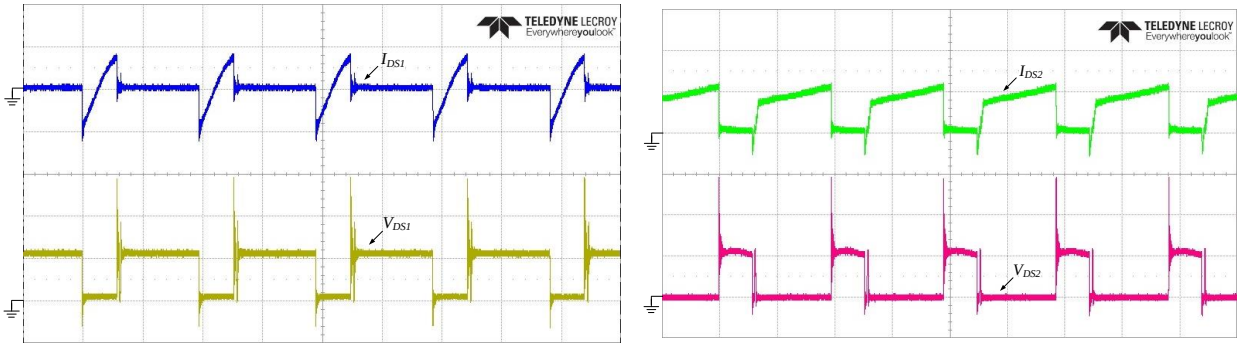

(**a**) (V_{DS1}: 20 V/div, I_{DS1}: 5 A/div, time: 10 μs/div) (**b**) (V_{DS2}: 20 V/div, I_{DS2}: 5 A/div, time: 10 μs/div)

Figure 21. Measured switch voltage V_{DS} and current I_{DS} waveforms under 30% of full-load condition: (**a**) switch M_1 and (**b**) switch M_2.

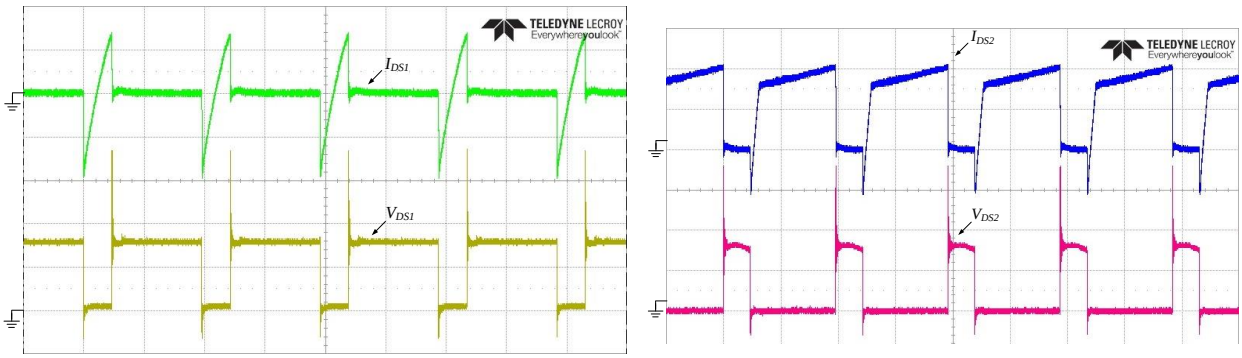

(**a**) (V_{DS1}: 20 V/div, I_{DS1}: 5 A/div, time: 10 μs/div) (**b**) (V_{DS2}: 20 V/div, I_{DS2}: 5 A/div, time: 10 μs/div)

Figure 22. Measured switch voltage V_{DS} and current I_{DS} waveforms under 100% of full-load condition: (**a**) switch M_1 and (**b**) switch M_2.

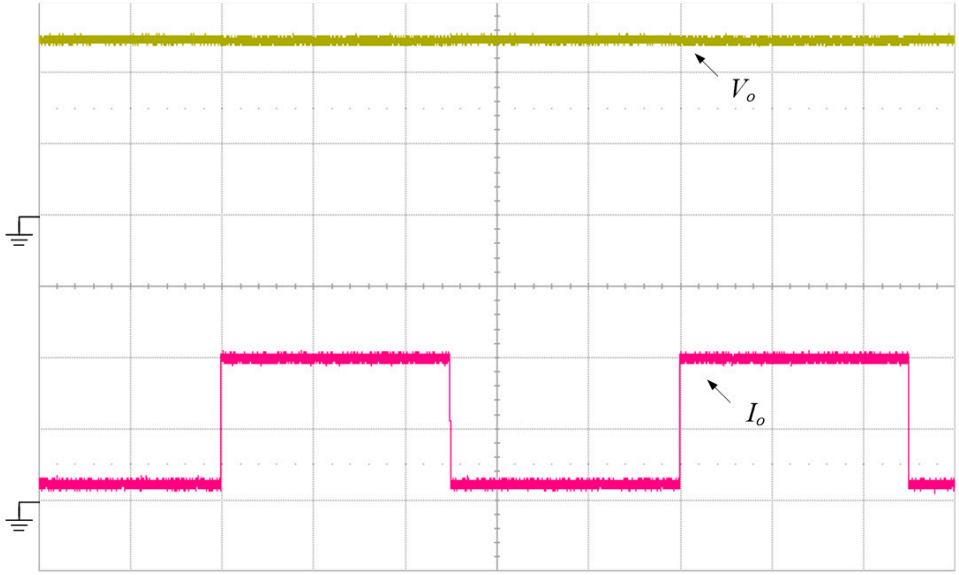

(V_o: 5 V/div, I_o: 2 A/div, time: 200 ms/div)

Figure 23. Measured output voltage V_o and current Io waveforms under step-load switching circuit from light load to heavy load.

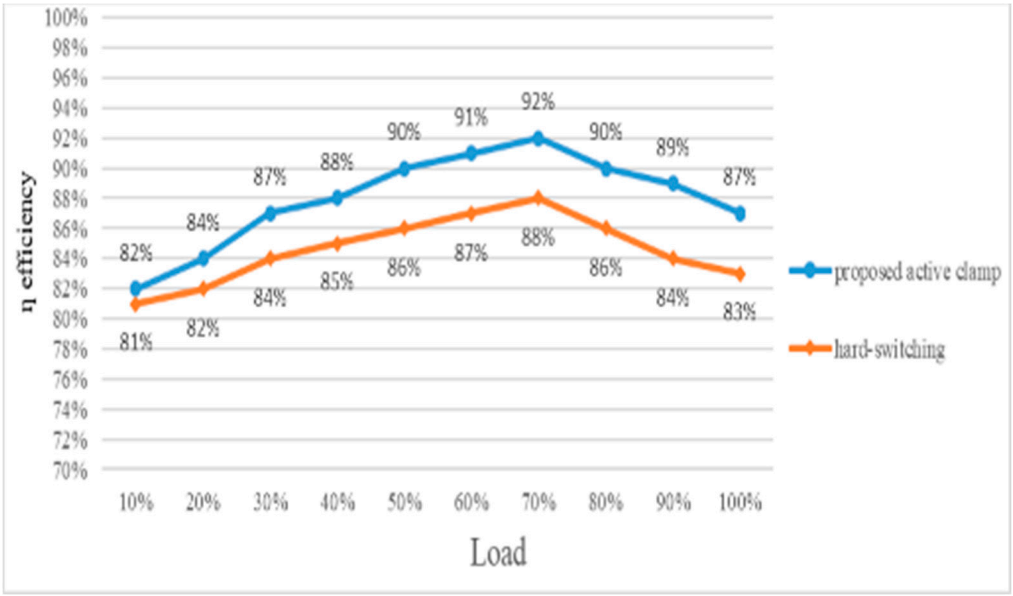

Figure 24. Conversion efficiency comparison between flyback converter with the proposed active clamp circuit and the one with hard-switching circuit from light load to heavy load.

7. Conclusions

The proposed zeta/flyback hybrid converter is regarded as the battery charger and discharger for solar power applications. In this paper, the degenerated circuit of the proposed hybrid converter is presented for reducing the components required. In addition, the circuit operational theorem, the circuit analyses, and the design of the proposed hybrid converter have been explained and derived in detail. From the experimental results, it can be seen that when the proposed hybrid converter operates in the charging condition, it can implement the MPPT of the solar power and charge the battery with the different charging current. Moreover, the proposed hybrid converter working in the discharging condition can be operated with ZVS at turn-on transition. The experimental results also showed that the conversion efficiency is 87% under 100 % of full-load condition, which

is increased by 4% as compared with the conventional counterparts with hard-switching circuit. A prototype of the proposed zeta/flyback hybrid converter has been implemented for lithium battery charger and driving LED lighting, respectively. The specifications of the maximum charging voltage and maximum charging current for lithium battery charger are 8.4V and 6 A, and the specifications of the output voltage and maximum output current for driving LED lighting are 12V and 4.2 A have been accomplished with the prototype to verify the feasibility of the proposed hybrid converter. Experimental results prove that the proposed hybrid is suitable for driving LED lighting.

Author Contributions: Conceptualization, S.-Y.T.; methodology, S.-Y.T.; software, S.-Y.T. and J.-H.F.; validation, S.-Y.T.; data curation, S.-Y.T.; writing—original draft preparation, S.-Y.T.; writing—review and editing, S.-Y.T.; visualization, S.-Y.T.; project administration, S.-Y.T. and J.-H.F. All authors have read and agreed to the published version of the manuscript.

Funding: This research was funded by MOST in Taiwan, grant number MOST 110-2221-E-182-040.

Institutional Review Board Statement: Not applicable.

Informed Consent Statement: Not applicable.

Data Availability Statement: Not applicable.

Conflicts of Interest: The authors declare no conflict of interest.

References

1. Castro, I.; Vazquez, A.; Aller, D.G.; Arias, M.; Lamar, D.G.; Sebastian, J. On Supplying LEDs from Very Low DC Voltages with High-Frequency AC-LED Drivers. *IEEE Trans. Power Electron.* **2019**, *34*, 5711–5719. [CrossRef]
2. Wang, Y.; Hu, X.; Guan, Y.; Xu, D. A Single-Stage LED Driver Based on Half-Bridge *CLCL* Resonant Converter and Buck–Boost Circuit. *IEEE Trans. Power Electron.* **2019**, *7*, 196–208. [CrossRef]
3. Tsou, M.-C.; Kuo, M.-T. Optimal Combination Design of a Light Emitting Diode Matrix Applicable to a Single-Stage Flyback Driver. *Energies* **2020**, *13*, 5209. [CrossRef]
4. Zhang, F.; Xie, Y.; Hu, Y.; Chen, G.; Wang, X. A Hybrid Boost–Flyback/Flyback Microinverter for Photovoltaic Applications. *IEEE Trans. Ind. Electron.* **2020**, *67*, 308–318. [CrossRef]
5. Lodh, T.; Pragallapati, N.; Agarwal, V. Novel Control Scheme for an Interleaved Flyback Converter Based Solar PV Microinverter to Achieve High Efficiency. *IEEE Trans. Ind. Appl.* **2018**, *54*, 3473–3482. [CrossRef]
6. Das, M.; Agarwal, V. Design and Analysis of a High-Efficiency DC–DC Converter with Soft Switching Capability for Renewable Energy Applications Requiring High Voltage Gain. *IEEE Trans. Ind. Electron.* **2016**, *63*, 2936–2944. [CrossRef]
7. Khodabandeh, M.; Afshari, E.; Amirabadi, M. A Family of Ćuk, Zeta, and SEPIC Based Soft-Switching DC–DC Converters. *IEEE Trans. Power Electron.* **2019**, *34*, 9503–9519. [CrossRef]
8. Tian, Q.; Zhou, G.; Liu, R.; Zhang, X.; Leng, M. Topology Synthesis of a Family of Integrated Three-Port Converters for Renewable Energy System Applications. *IEEE Trans. Ind. Electron.* **2021**, *68*, 5833–5846. [CrossRef]
9. Banaei, M.R.; Sani, S.G. Analysis and Implementation of a New SEPIC-Based Single-Switch Buck–Boost DC–DC Converter with Continuous Input Current. *IEEE Trans. Power Electron.* **2018**, *33*, 10317–10325. [CrossRef]
10. Liu, X.; Wan, Y.; Dong, Z.; He, M.; Zhou, Q.; Tse, C.K. Buck–Boost–Buck-Type Single-Switch Multistring Resonant LED Driver with High Power Factor and Passive Current Balancing. *IEEE Trans. Power Electron.* **2020**, *35*, 5132–5143. [CrossRef]
11. Tseng, S.-Y.; Fan, J.-H. Buck-Boost/Flyback Hybrid Converter for Solar Power System Applications. *Electronics* **2021**, *10*, 414. [CrossRef]
12. Cao, Y.; Li, K.; Lu, M. Balancing Method Based on Flyback Converter for Series-Connected Cells. *IEEE Access* **2021**, *9*, 52393–52403. [CrossRef]
13. Guo, X.; Geng, J.; Liu, Z.; Xu, X.; Cao, W. A Flyback Converter-Based Hybrid Balancing Method for Series-Connected Battery Pack in Electric Vehicles. *IEEE Trans. Veh. Technol.* **2021**, *70*, 6626–6635. [CrossRef]
14. Yuan, Y.; Lai, L.; Wu, Q.; Yi, C. An Integrated Boost-LC-Resonant-Flyback Multimode Converter for Battery Charger Applications. *IEEE Trans. Ind. Electron.* **2021**, *68*, 5686–5689. [CrossRef]
15. Ravi, V.; Satpathy, S.; Lakshminarasamma, N. An Energy-Based Analysis for High Voltage Low Power Flyback Converter Feeding Capacitive Load. *IEEE Trans. Power Electron.* **2021**, *35*, 546–564. [CrossRef]
16. Kumar, M.; Babu, Y.N.; Pullaguram, D.; Mishra, S. A high voltage gain non-isolated modified three-port DC/DC converter based on integrated Boost-Cuk topology. In Proceedings of the 2017 IEEE PES Asia-Pacific Power and Energy Engineering Conference (APPEEC), Bangalore, India, 8–10 November 2017; pp. 1–6.
17. Wu, H.; Zhang, J.; Xing, Y. A Family of Multiport Buck–Boost Converters Based on DC-Link-Inductors (DLIs). *IEEE Trans. Power Electron.* **2015**, *30*, 735–746. [CrossRef]

18. Wu, Y.-E.; Chiu, P.-N. A High-Efficiency Isolated-Type Three-Port Bidirectional DC/DC Converter for Photovoltaic Systems. *Energies* **2017**, *10*, 434. [CrossRef]
19. Manoharan, P.; Subramaniam, U.; Babu, T.S.; Padmanaban, S.; Holm-Nielsen, J.B.; Mitolo, M.; Ravichandran, S. Improved Perturb and Observation Maximum Power Point Tracking Technique for Solar Photovoltaic Power Generation Systems. *IEEE Syst. J.* **2021**, *15*, 3024–3035. [CrossRef]